The Astrophysical Journal, 1004:31 (16pp), 2026 June 10 https://doi.org/10.3847/1538-4357/ae66fd

A Path to Constraints on Common Envelope Ejection in Massive Binaries: Full Evolutionary Reconstruction of Three Black Hole X-Ray Binaries

Zhenwei Li[1,2], Dandan Wei[3], Shi Jia[1,2], Hailiang Chen[1,2], Hongwei Ge[1,2], Zhuo Chen[4], Yangyang Zhang[5], Xuefei Chen[1,2], and Zhanwen Han[1,2]

[1] International Centre of Supernovae (ICESUN), Yunnan Key Laboratory of Supernova Research, Yunnan Observatories, Chinese Academy of Sciences (CAS), Kunming 650216, People's Republic of China; lizw@ynao.ac.cn, gehw@ynao.ac.cn, cxf@ynao.ac.cn
[2] University of Chinese Academy of Sciences, Beijing 100049, People's Republic of China
[3] Institute of Science and Technology Austria (ISTA), Am Campus 1, 3400 Klosterneuburg, Austria
[4] Institute for Advanced Study, Tsinghua University, Beijing 100084, People's Republic of China
[5] Zhoukou Normal University, East Wenchang Street, Chuanhui District, Zhoukou, 466001, People's Republic of China
Received 2026 March 24; revised 2026 April 22; accepted 2026 April 25; published 2026 June 3

Abstract

The massive binary common envelope (CE) phase plays a pivotal role in the formation of close black hole (BH)/neutron star binaries, yet significant uncertainties remain in our understanding of this process. In this study, we aim to constrain the massive binary CE phase by systematically reconstructing three observed BH X-ray binaries (BHXBs): GRO J1655-40, SAX J1819.3-2525, and 4U 1543-47. Through comprehensive binary evolution simulations and parametric supernova modeling, we establish lower limits for the CE efficiency parameters under different energy considerations within the standard energy formalism. Specifically, we derive minimum values for three cases: $\alpha_{0.5U}$ and α_{U}, representing CE efficiencies with half and all of the internal energy contributing to the envelope ejection, respectively, and α_{H}, accounting for the envelope's enthalpy. Our analysis reveals that the self-consistent formation of these three BHXBs requires CE efficiency parameters satisfying $\alpha_{0.5U} \gtrsim 6.7$, $\alpha_{U} \gtrsim 4.2$, and $\alpha_{H} \gtrsim 1.7$. Notably, we find no viable solutions with CE efficiency values below unity, even when considering the most extreme scenarios, in which the envelope binding energy is significantly reduced through enthalpy inclusion. Our results strongly imply that either additional energy sources are required or the formalism itself must be revised. Furthermore, we quantitatively assess the impact of BH natal kicks on our results. A key finding is that 4U 1543-47's formation requires substantial natal kicks ($\gtrsim$50 km s^{-1}), as lower kick velocities are incompatible with isolated binary evolution.

Unified Astronomy Thesaurus concepts: Binary stars (154); Common envelope evolution (2154); X-ray binary stars (1811)

1. Introduction

Binary star systems are ubiquitous in the Universe, with observational studies suggesting that a significant fraction of stellar systems exist in binary or multiple configurations (H. Sana et al. 2012; M. Moe & R. Di Stefano 2017; Y. Guo et al. 2022; X. Chen et al. 2024). The evolution of binary systems plays a pivotal role in understanding various astrophysical phenomena, including the formation of compact object binaries, type Ia supernova (SN) progenitors, and X-ray binary systems (O. De Marco & R. G. Izzard 2017; Z.-W. Han et al. 2020; D. Belloni & M. R. Schreiber 2023; Z.-W. Liu et al. 2023; T. M. Tauris & E. P. J. van den Heuvel 2023; X. Chen et al. 2024). Despite remarkable theoretical and observational advances in recent decades, fundamental challenges remain in our understanding of binary evolution processes. Among these, common envelope (CE) evolution stands out as one of the most critical yet poorly understood phases, serving as a key mechanism for producing cataclysmic variables, ultracompact X-ray binaries, and binary gravitational-wave sources (see the reviews by N. Ivanova et al. 2013, 2020; F. K. Röpke & O. De Marco 2023).

Although significant effort has been devoted to modeling CE evolution through numerical simulations spanning 1D to 3D approaches (e.g., N. Ivanova & J. L. A. Nandez 2016; M. U. Kruckow et al. 2016; S. T. Ohlmann et al. 2016; N. Soker 2016; R. Iaconi et al. 2017; L. Chamandy et al. 2018; S. Shiber & N. Soker 2018; T. Fragos et al. 2019; S. Shiber et al. 2019; J. A. P. Law-Smith et al. 2020; A. Grichener et al. 2021; M. Y. M. Lau et al. 2022; M. M. Moreno et al. 2022; V. A. Bronner et al. 2024; D. Gagnier & O. Pejcha 2025; M. Vetter et al. 2025), the astrophysical community has largely adopted a phenomenological description based on energy conservation as a practical framework for modeling the CE ejection (B. Paczynski 1976; R. F. Webbink 1984; M. Livio & N. Soker 1988). In this energy formalism,[6] the system's orbital energy release is assumed to overcome the envelope's binding energy. This approach offers significant advantages: its simplicity and computational efficiency make it particularly suitable for population synthesis studies (see the recent reviews by Z.-W. Han et al. 2020; X. Chen et al. 2024).

The CE ejection efficiency α_{CE}, representing the fraction of orbital energy actually used to eject the envelope, remains one

[6] In the remainder of this paper, the CE energy formalism refers to the standard version used in binary population synthesis studies. It therefore does not consider additional processes or energy sources that may operate during the CE phase, including but not limited to jets (e.g., N. Soker 2004, 2015, 2016; S. Shiber et al. 2019), magnetic fields (e.g., S. T. Ohlmann et al. 2016; G. García-Segura et al. 2020), and nuclear energy (P. Podsiadlowski et al. 2010).

of the most crucial yet poorly constrained parameters in CE evolution. As a free parameter in theoretical models, $\alpha_{\rm CE}$ proves difficult to determine from numerical simulations alone. Analysis of post-CE systems, especially close white dwarf and hot subdwarf binaries, currently provides the most reliable constraints on the CE efficiency (e.g., M. Zorotovic et al. 2010; O. De Marco et al. 2011; P. J. Davis et al. 2012; A. Rebassa-Mansergas et al. 2012; R. Iaconi & O. De Marco 2019; H. Ge et al. 2022, 2024b; M. S. Hernandez et al. 2022; M. Zorotovic & M. Schreiber 2022; P. Scherbak & J. Fuller 2023; D. Belloni et al. 2024a, 2024b; N. Yamaguchi et al. 2024; Y. Zhang et al. 2024; S. Torres et al. 2025). These analyses reveal two consistent trends: (1) the majority of post-CE white dwarf binaries require only modest $\alpha_{\rm CE}$ values (<1); and (2) the efficiency appears to vary systematically with progenitor system properties, showing strong dependencies on both initial masses and orbital periods (O. De Marco et al. 2011; P. J. Davis et al. 2012; H. Ge et al. 2022, 2024b; Y. Zhang et al. 2024).

Post-CE systems containing white dwarfs or hot subdwarfs primarily originate from binaries with intermediate- and low-mass donors ($\lesssim 8\,M_{\odot}$). In contrast, CE evolution involving massive stars ($\gtrsim 8\,M_{\odot}$) presents significantly greater complexity, due to both theoretical and observational challenges. Theoretically, uncertainties persist regarding the structure and evolution of massive stars, including (but not limited to) their stellar winds, SN explosion mechanisms, and compact remnant natal kicks (J. Vink 2012; J. S. Vink 2022; P. Marchant & J. Bodensteiner 2024; D. Wei et al. 2024). Observationally, post-CE systems descended from massive progenitors remain exceptionally rare (Y. Götberg et al. 2023; Z. L. Yang et al. 2025). These combined factors have led to particularly poor constraints on CE evolution in massive binary systems.

Current understanding suggests that massive stellar envelopes are significantly more difficult to eject than their low-mass counterparts (E. Pfahl et al. 2003; P. Podsiadlowski et al. 2003, 2010; S. Justham et al. 2006; P. D. Kiel & J. R. Hurley 2006; L. R. Yungelson et al. 2006; G. Wiktorowicz et al. 2014; Z.-Y. Zuo & X.-D. Li 2014; X.-D. Li 2015; Y. Shao & X.-D. Li 2015; C. Wang et al. 2016a, 2016b; T. Fragos et al. 2019; E. C. Wilson & J. Nordhaus 2022). This challenge primarily stems from the substantial radiative envelopes surrounding massive stellar cores, which dramatically increase the total binding energy (X.-J. Xu & X.-D. Li 2010; C. Wang et al. 2016a, 2016b; R. Hirai & I. Mandel 2022; E. C. Wilson & J. Nordhaus 2022; L. Picker et al. 2024). To account for this difficulty, binary population synthesis studies of massive systems often employ (equivalent) CE efficiency[7] values as high as $\alpha_{\rm CE} \sim 3-10$ (M. Dominik et al. 2012; M. M. Briel et al. 2023; A. Grichener 2023; A. M. Tanaka et al. 2023; Z.-L. Deng et al. 2024; Y.-D. Nie et al. 2025). Notably, the adopted CE efficiency dramatically impacts the predicted merger rates of double compact objects, introducing uncertainties spanning 2–3 orders of magnitude (M. Dominik et al. 2012; M. U. Kruckow et al. 2018; A. Grichener 2023; A. M. Tanaka et al. 2023). It becomes fundamentally important to constrain CE efficiency parameters in massive binary systems.

In this study, we establish constraints on the CE efficiency for massive binaries by analyzing three observed black hole intermediate-mass X-ray binaries (BH-IMXBs)—systems believed to be products of CE evolution (see Section 2 for detailed descriptions). Our approach combines detailed binary evolution simulations with a parametric SN model, enabling us to reconstruct the complete evolutionary history of these selected BH-IMXBs in a self-consistent framework. The derived lower limits on the CE efficiency values will provide crucial inputs for future population synthesis studies of massive binary systems.

The remainder of this paper is structured as follows. Section 2 details our simulation methods and key input parameters. In Section 3, we present the simulated parameter grids for the three BH X-ray binaries (BHXBs), derive constraints on the CE efficiency values, and analyze the impact of BH natal kicks. Finally, Sections 4 and 5 discuss our findings and present conclusions, respectively.

2. Methods

2.1. Observed Parameters of the Chosen BHXBs

This study investigates the CE phase in massive binaries through analysis of three dynamically confirmed BH-IMXBs with well-constrained system parameters (Table 1)—i.e., GRO J1655-40 (hereafter, GRO J1655), SAX J1819.3-2525 (hereafter, SAX J1819), and 4U 1543-47 (hereafter, 4U 1543). These systems were selected based on the following criteria: (1) Galactic disk localization (J. M. Corral-Santana et al. 2016; B. E. Tetarenko et al. 2016; F. Fortin et al. 2024), suggesting isolated binary evolution origins; and (2) extreme initial mass ratios of the primordial binaries indicating probable CE evolution (see Section 2.2 for details). Our focus on BH-IMXBs rather than BH low-mass XBs (BH-LMXBs; Q. Z. Liu et al. 2007; J. M. Corral-Santana et al. 2016) is motivated by two key factors: (1) the magnetic braking processes play a vital role in the formation of BH-LMXBs, and the uncertain magnetic braking processes introduce significant errors in post-CE orbital separation estimates (Section 2.3; Z.-L. Deng & X.-D. Li 2024); and (2) the substantial mass loss in low-mass companions (W.-C. Chen & X.-D. Li 2006; S. Justham et al. 2006; X.-D. Li 2008) and associated progenitor mass uncertainties would dramatically increase computational requirements.

2.2. Formation Scenario of BHXBs

Figure 1 presents the typical evolutionary sequence for BHXB formation through isolated binary evolution, beginning with a primordial system containing a massive primary ($M_1 \gtrsim 32\,M_{\odot}$, based on the parametric SN models; Section 2.4) and a lower-mass secondary ($M_2 \lesssim 6.2\,M_{\odot}$, from the binary simulations below in Section 3.1; Stage 1). The primary evolves off the main sequence (MS) after forming a helium (He) core, initiating Roche lobe overflow with a mass ratio $\gtrsim 5$ (Stage 2) that leads to dynamically unstable mass transfer (H. Ge et al. 2020a, 2020b, 2024a) and a subsequent CE phase (Stage 3). Successful CE ejection—an essential requirement for BHXB formation—leaves a stripped He star and a nearly unevolved MS companion (Stage 4). The He star then loses significant mass through stellar winds (Stage 5), before undergoing core collapse to form a BH via SN fallback (Stage 6). Finally, as the secondary evolves and fills its Roche

[7] The binding energy parameter λ is commonly introduced, with the product $\alpha_{\rm CE}\lambda$ representing the combined effects of envelope binding energy and ejection efficiency (M. de Kool et al. 1987). Some studies have adopted high λ values while maintaining modest $\alpha_{\rm CE}$.

Table 1
The Binary Parameters of the Three BHXBs

Name	$P_{\rm orb}$ (hr)	$M_{\rm BH}$ ($M_\odot$)	M_2 ($M_\odot$)	$T_{\rm eff}$ (K)	$a_{\rm BH}$	References
GRO J1655[a]	62.920	6.3 ± 0.5	2.4 ± 0.4	5715−5990	0.7 ± 0.05	(1)
SAX J1819	67.6152	6.4 ± 0.6	2.9 ± 0.4	12,261−12,461	⋯	(2)
4U 1543	26.79377	9.4 ± 2.0	2.63 ± 0.24	9000 ± 500	$0.67^{+0.15}_{-0.08}$	(3)

Notes.
[a] M. E. Beer & P. Podsiadlowski (2002) suggested another set of constraints with $M_{\rm BH} = 5.4 \pm 0.4\,M_\odot$ and $M_2 = 1.45 \pm 0.35\,M_\odot$ for GRO J1655 (see also S. E. Motta et al. 2014).
References: (1) J. A. Orosz & C. D. Bailyn (1997); J. Greene et al. (2001); T. Shahbaz (2003); R. Shafee et al. (2006); (2) J. A. Orosz et al. (2001); R. K. D. MacDonald et al. (2014); and (3) J. A. Orosz et al. (1998); J. A. Orosz (2003); B. E. Tetarenko et al. (2016); Y. Dong et al. (2020).

lobe, accretion onto the BH produces X-ray emission, completing the formation of an observable BHXB system (Stage 7).

2.3. The Technical Route

The formation of BHXBs[8] requires the progenitor binary to undergo a CE phase, which is generally described by the classical energy formalism (R. F. Webbink 1984; M. Livio & N. Soker 1988). This mechanism relates the envelope's binding energy to the change in orbital energy through

$$E_{\rm bind} = \alpha_{\rm CE}\left(-\frac{GM_{1,s3}M_2}{2a_{\rm pre-CE}} + \frac{GM_{1c,s3}M_2}{2a_{\rm post-CE}}\right), \quad (1)$$

where $E_{\rm bind}$ represents the envelope binding energy at the onset of the CE phase; $M_{1,s3}$, $M_{1\,c,s3}$ are for the masses of the primary and primary's core, respectively, at Stage 3; and $a_{\rm pre-CE}$, $a_{\rm post-CE}$ are the orbital separation before and after the CE ejection phase, respectively. To constrain the CE efficiency $\alpha_{\rm CE}$, we must determine the binary parameters at two critical evolutionary steps: (1) the pre-CE phase when the primary fills its Roche lobe (Stage 3); and (2) the post-CE phase, consisting of a newly formed He star and an unevolved (nearly) MS companion (Stage 4). Our methodology integrates both detailed single-star evolutionary calculations and comprehensive binary star simulations to consistently model the system's evolution across these key phases.

Step 1—determining the pre-CE binary parameters ($M_{1,s3}$, $M_{1\,c,s3}$, and $a_{\rm pre-CE}$, $E_{\rm bind}$). We first conduct single-star simulations for the BH progenitor (see Section 2.4). When the star develops an He core and initiates Roche lobe overflow, we calculate the pre-CE orbital separation ($a_{\rm pre-CE}$) via (P. P. Eggleton 1983)

$$a_{\rm pre-CE} = R_{1,\rm L}\frac{0.6q_{s3}^{2/3} + \ln(1 + q_{s3}^{1/3})}{0.49q_{s3}^{2/3}}, \quad (2)$$

where $R_{1,\rm L} \approx R_{1,s3}$, $R_{1,s3}$ is the primary's radius at Stage 3, $q_{s3} = M_{1,s3}/M_2$ is the mass ratio, and M_2 is the companion mass determined from binary evolution simulations (described below).

We employ three distinct approaches to compute the envelope binding energy ($E_{\rm bind}$) of the donor star at Stage 3. For Cases 1 and 2, we calculate $E_{\rm bind}$ using the standard energy integral:

$$E_{\rm bind} = -\int_{\rm core}^{\rm surface}\left(-\frac{Gm}{r} + \alpha_{\rm th}U\right)dm, \quad (3)$$

where U represents the internal energy, including thermal and recombination energy (Z. Han et al. 1994; C. Wang et al. 2016a; J. Klencki et al. 2021; P. Marchant et al. 2021). $\alpha_{\rm th}$ denotes the fraction of the internal energy contributing to envelope ejection. We adopt $\alpha_{\rm th} = 0.5$ (Case 1) and 1 (Case 2).

For our third treatment (Case 3), we incorporate the "*enthalpy*" term in the binding energy calculation, following N. Ivanova & S. Chaichenets (2011):

$$E_{\rm bind} = -\int_{\rm core}^{\rm surface}\left(-\frac{Gm}{r} + U + \frac{P}{\rho}\right)dm, \quad (4)$$

where P and ρ represent the pressure and density, respectively, of each mass shell. The quantity $U + P/\rho$ is generally known as *enthalpy* (H). It should be noted that the enthalpy consideration does not introduce new energy sources, but rather redistributes the deposited heat during the spiral-in phase (N. Ivanova & S. Chaichenets 2011; N. Ivanova et al. 2013). Following N. Ivanova (2011), we define the core–envelope boundary as the point with the maximum compression P/ρ inside the hydrogen burning shell (characterized by the peak values of the local sonic velocity; see also P. Marchant et al. 2021; A. Vigna-Gómez et al. 2022)—a choice motivated by the need to prevent the donor remnant from expanding immediately after CE ejection.

Figure 2 illustrates our binding energy calculation methodology for an initial $34\,M_\odot$ star. Panel (a) shows the evolutionary track in the H-R diagram, with the red cross marking the specific evolutionary stage analyzed in panel (b). In panel (b), we present the radial profiles of the hydrogen (H) mass fraction and the sonic velocity $C_{\rm s} \equiv \sqrt{P/\rho}$, where we identify the core–envelope boundary at the $C_{\rm s}$ extremum ($X_{\rm H} \approx 0.18$), yielding a core mass of $\sim$13.5 $M_\odot$. Panel (c) shows the evolution of the primary envelope energy components—the gravitational energy ($E_{\rm gr}$), internal energy ($E_{\rm U}$), and enthalpy ($E_{\rm H}$)—as functions of stellar radius, where the radius corresponds to each specific evolutionary stage, covering the stages following the formation of an He core, i.e., post-MS. The resulting binding energies for all three cases appear in panel (d). We see that Cases 1 and 2 exhibit a decreasing binding energy with stellar expansion, while Case 3 maintains a relatively constant binding energy throughout the

[8] Throughout the remainder of this paper, the term "BHXB" refers specifically to BH-IMXBs.

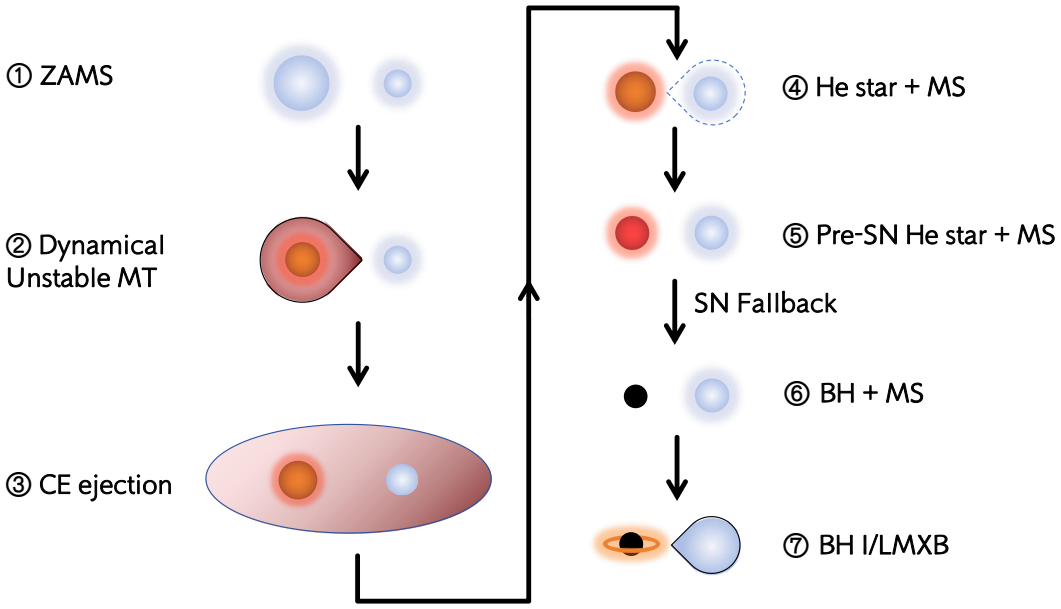

Figure 1. The typical evolutionary scenario for BH-IMXBs/BH-LMXBs. The abbreviations are as follows: ZAMS—zero-age MS; and MT—mass transfer. At Stage 4, the dashed contour denotes the Roche lobe of the secondary star. Note that the successful ejection of the CE requires the secondary's radius to be within its Roche lobe.

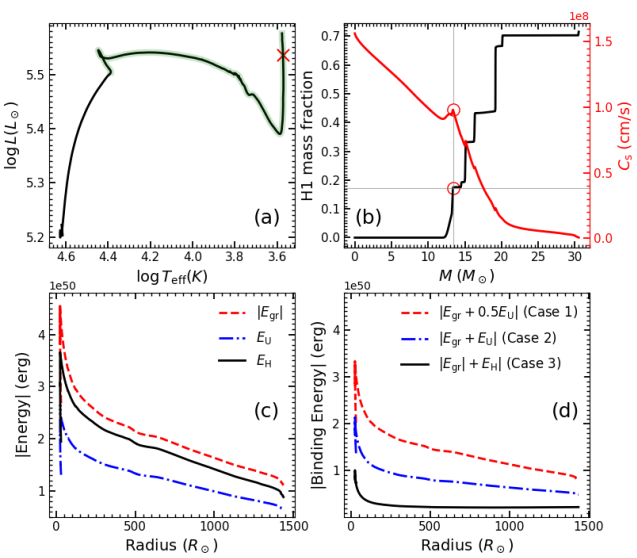

Figure 2. Binding energy calculation example for a 34 $M_\odot$ primary star. Panel (a): the evolutionary track in the H-R diagram with the red cross indicating the specific evolutionary stage analyzed. The thick green line indicates that the star contains an He core. Panel (b): radial profiles of the hydrogen mass fraction (X_H) and the sonic velocity $C_s \equiv \sqrt{P/\rho}$ at this stage, where the open circles mark the core–envelope boundary. Panel (c): the evolution of the primary envelope energy components (gravitational energy E_{gr}, internal energy E_U, and enthalpy term E_H), as functions of stellar radius at each specific evolutionary stage (covering the post-MS stages). Panel (d): similar to panel (c), but for the integrated envelope binding energy versus radius for the three cases.

late expansion phase, which is similar to what was observed by C. Wang et al. (2016a).

Step 2—determining the post-CE binary parameters ($a_{\rm post-CE}$, M_2). We conduct a series of binary star evolutionary calculations for BH + MS systems (Stage 6), screening the parameter space to identify models that match the observational BHXB data within uncertainties (similar to the methods of B. Willems et al. 2005; T. Fragos et al. 2009; T.-W. Wong et al. 2012, 2014; M. Sørensen et al. 2017). For each viable model in the parameter space, we determine the BH mass ($M_{\rm BH}$), companion mass (M_2), and orbital separation (a_{s6}) at Stage 6, then derive the corresponding post-CE (Stage 4) parameters. A system is considered successfully reproduced when its evolutionary track simultaneously matches the three observed parameters ($M_{\rm BH}$, M_2, and the orbital period $P_{\rm orb}$) within their error ranges. To account for theoretical uncertainties in the period predictions arising from imperfect knowledge of angular momentum loss mechanisms, mass-loss processes, and tidal interactions (see, e.g., T. M. Tauris & E. P. J. van den Heuvel 2006; K. A. Postnov & L. R. Yungelson 2014), we adopt a conservative 50% uncertainty on the modeled orbital periods relative to the observed values.

From Stage 6 to Stage 5, the binary parameters are affected by the SN explosion event during the BH formation. Our default model assumes zero BH natal kick for simplicity. Under this framework, we apply the Blaauw–Boersma formalism (A. Blaauw 1961; J. Boersma 1961) to describe the instantaneous mass loss during the SN event, while neglecting any natal kick to the BH remnant. Assuming that the sudden mass loss does not affect the binary position and relative velocity at the moment of the SN event, the eccentricity e induced by the mass loss and the new semi-axis a_p just after the SN event are given by $e = (M_{\rm pre-SN} - M_{\rm BH})/(M_{\rm BH} + M_2)$, $a_p = a_{s5}/(1 - e)$ (R. J. Dewey & J. M. Cordes 1987; F. Verbunt et al. 1990), where a_{s5} is the binary separation at Stage 5. We further assume that the orbit is rapidly circularized after the SN event (F. Verbunt et al. 1990); based on the angular momentum conservation, the circularized orbit satisfies $a_{s6} = (1 - e^2)a_p$. Consequently, we obtain

$$\frac{a_{s6}}{a_{s5}} = \frac{M_{\rm pre-SN} + M_2}{M_{\rm BH} + M_2}. \quad (5)$$

The pre-SN He star mass $M_{\rm pre-SN}$ relates to the initial He star mass $M_{\rm He}$ (equivalent to the post-CE core mass $M_{1\,c,s3}$)

through the empirical relation derived from detailed stellar evolution models S. E. Woosley (2019):

$$M_{\rm pre-SN} = 0.463\, M_{\rm He} + 1.49\, M_{\odot}. \quad (6)$$

From Stage 5 to Stage 4, the orbit evolution is governed by mass loss through the stripped He star's stellar wind, which we consider as a fast (several thousands of $\rm km\,s^{-1}$; J. S. Vink 2022) and isotropic spherically symmetric wind that does not interact with the companion star. The assumptions are well justified for Wolf–Rayet stars where the wind velocity significantly exceeds the typical orbital velocity ($\sim$100 $\rm km\,s^{-1}$), making wind accretion negligible (I. El Mellah et al. 2019; Z. Li et al. 2026). The change in binary separation due to the wind mass loss then is given by (K. A. Postnov & L. R. Yungelson 2014)

$$\frac{a_{\rm s5}}{a_{\rm post-CE}} = \frac{M_{\rm He} + M_2}{M_{\rm pre-SN} + M_2}. \quad (7)$$

For each set of binary parameters at Stage 6 that successfully reproduces the observed BHXB properties, we can systematically reconstruct the corresponding post-CE binary configuration at Stage 4. Using Equation (1), together with the binding energy $E_{\rm bind}$ calculated for a given BH progenitor across different evolutionary stages, we determine the required CE efficiency parameter $\alpha_{\rm CE}$ for each viable solution.

It should be noted that these calculations adopt the Blaauw–Boersma formalism, which neglects natal kicks. The potential impact of nonzero kick velocities on our results will be examined in Section 3.2.

2.4. The BH Progenitors

The formation of a BH is strongly linked to pre-SN stellar structures and explosion mechanisms, with current simulations revealing a complex nonlinear relationship between the progenitor mass and final BH mass (H.-T. Janka 2012; M. Ugliano et al. 2012; T. Ertl et al. 2016; H.-T. Janka et al. 2016; T. Sukhbold et al. 2016). This complexity is further compounded in binary systems, where interactions significantly alter pre-SN structures and consequently affect SN outcomes (E. Laplace et al. 2021, 2025; F. R. N. Schneider et al. 2021, 2023, 2024, 2025; D. Vartanyan et al. 2021; D. R. Aguilera-Dena et al. 2023). Recently, F. R. N. Schneider et al. (2021) combined detailed pre-SN simulations with the parametric explosion model of B. Müller et al. (2016) to predict stellar fates while accounting for binary interactions with three distinct cases of envelope stripping: Case A (during core H burning), Case B (during H-shell burning), and Case C (after core He burning). Rather than simulating SN explosions directly, we utilize the results of F. R. N. Schneider et al. (2021) to determine whether a star collapses to form a BH (see also Section 2.5).

We assume the CE phase occurs when the donor star has developed an He core but before core He ignition (for Case B stripped stars, following the He ignition in the core, the stellar radius undergoes rapid shrinkage; J. Klencki et al. 2021). This assumption of CE occurrence before maximum radial expansion is observationally justified when tidal effects are not too strong (e.g., J. D. Nie et al. 2017; see Section 4 for further discussion). According to F. R. N. Schneider et al. (2021), Case B stripped stars produce BHs through three distinct mass ranges: $\sim$32−40 $M_{\odot}$, $\sim$46−60 $M_{\odot}$, and $\sim$70−100 $M_{\odot}$. The most massive progenitors (70−100 $M_{\odot}$) undergo direct collapse, typically forming BHs exceeding 10 $M_{\odot}$, which are heavier than those in our sample (Table 1). Lower-mass progenitors (33−60 $M_{\odot}$) generally form lighter BHs via fallback accretion. In the 32 $M_{\odot}$ case, although direct collapse occurs due to enhanced CO core compaction, the resulting BH mass remains below $\sim$8 $M_{\odot}$, depending on the gravitational binding energy release. Based on these findings, we constrain our analysis to progenitor masses of 32–40 $M_{\odot}$ and 46–60 $M_{\odot}$ for the three BHXBs.

2.5. The Input Parameters

We perform all stellar evolution calculations using the state-of-the-art stellar evolutionary code Modules for Experiments in Stellar Astrophysics (MESA, version 12115; B. Paxton et al. 2011, 2013, 2015, 2018, 2019; A. S. Jermyn et al. 2023), adopting solar metallicity ($Z = 0.0142$) with an initial He fraction $Y = 0.2703$ (M. Asplund et al. 2009) for nonrotating massive star models (as the strong stellar winds in massive stars cause a marked spindown; e.g., K. Nathaniel et al. 2025). Our simulations incorporate type II opacities (C. A. Iglesias & F. J. Rogers 1996) and the approx21_cr60_plus_co56.net nuclear reaction network (J. W. Ferguson et al. 2005), with convection parameters including a mixing length of $\alpha_{\rm mlt} = 1.8$, core overshooting of 0.2 pressure scale heights during H/He burning phases (R. J. Stancliffe et al. 2015), and semiconvection efficiency $\alpha_{\rm sc} = 0.1$ (J. Choi et al. 2016). Stellar wind mass loss follows the prescriptions of P. Marchant et al. (2016). These chosen input parameters are closely similar to those employed by F. R. N. Schneider et al. (2021), ensuring consistency when applying their results to determine BH progenitor masses.

Our binary evolution simulations focus specifically on the formation of BHXBs from BH + MS systems. In this framework, we model the BH as a nonrotating point mass while evolving the MS star using the same physical prescriptions described previously. The BH accretion is limited by the Eddington accretion rate, i.e.:

$$\dot{M}_{\rm Edd} = \frac{4\pi G M_{\rm BH}}{\kappa c \eta} \simeq 2.6 \times 10^{-7} M_{\odot}\,{\rm yr}^{-1} \left(\frac{M_{\rm BH}}{10 M_{\odot}}\right)\left(\frac{\eta}{0.1}\right)^{-1}\left(\frac{1+X}{1.7}\right)^{-1}, \quad (8)$$

where $\kappa (\equiv 0.2(1 + X) {\rm cm^2\,g^{-1}})$ is the electron scattering opacity (R. Kippenhahn & A. Weigert 1990), c is the speed of light, and η is the accretion efficiency, which is approximately given by (P. Podsiadlowski et al. 2003)

$$\eta = 1 - \sqrt{1 - \left(\frac{M_{\rm BH}}{3 M_{\rm BH,0}}\right)}, \quad (9)$$

where $M_{\rm BH,0}$ and $M_{\rm BH}$ are the initial and the present mass of the BH, respectively. The unprocessed material is assumed to carry away the specific angular momentum of the BH as irradiation wind (K. A. Postnov & L. R. Yungelson 2014).

In our binary evolution calculations, we systematically explore the parameter space by varying three key parameters: (1) the initial BH mass at Stage 6, which we sample from 3.0 $M_{\odot}$ upward in increments of 0.3 $M_{\odot}$, until exceeding the observed values; (2) the companion star mass M_2, ranging from the lower observational limit to the maximum value

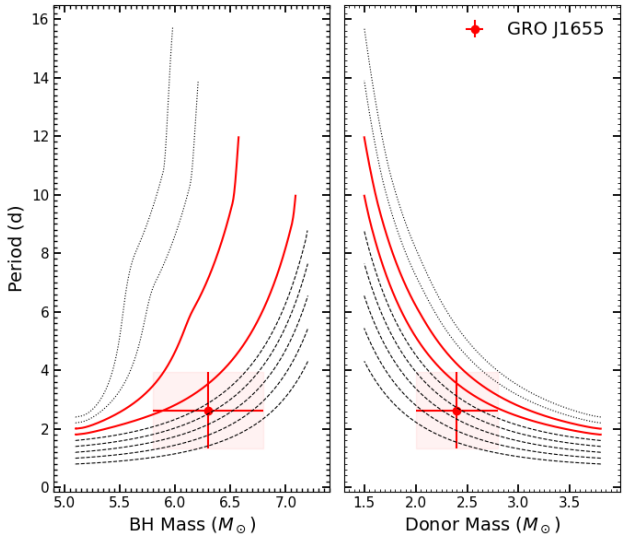

Figure 3. Binary evolutionary tracks for GRO J1655. The initial binary systems have $M_{\rm BH} = 5.1\,M_\odot$, $M_2 = 3.8\,M_\odot$, and orbital periods spanning from 0.8 to 2.4 days in a step of 0.2 days. Two classes of solutions successfully reproduce the observed $M_{\rm BH}$, $M_{\rm donor}$, and $P_{\rm orb}$: (1) forbidden configurations (black dashed lines), where the MS star would fill its Roche lobe during post-CE evolution (Stage 4 in Figure 1); and (2) physically allowable solutions (red solid lines) that avoid this constraint. The black dotted lines represent binary configurations that fail to reproduce GRO J1655's observed parameters.

capable of reproducing the observed systems, also in $0.3\,M_\odot$ steps; and (3) the initial orbital period at Stage 6, covering 0.6 −5.0 days, with an interval of 0.2 days for GRO J1655 and SAX J1819, and a finer stepping of 0.1 days for 4U 1543, to account for its tighter observational constraints.

3. Results

3.1. Binary Grids for BHXBs

Figure 3 presents a representative set of evolutionary tracks for GRO J1655, where we fix the initial BH mass at $5.1\,M_\odot$ and the secondary mass at $3.8\,M_\odot$, while varying the orbital period from 0.8 days to 2.4 days in a step of 0.2 days. During the mass-transfer phase, both the orbital periods and BH masses increase as the donor star loses mass. Among these models, the first seven binaries (black dashed and red solid lines) successfully traverse the observational parameter space of GRO J1655, while systems with longer initial periods (dotted lines) fail to reproduce the observed system, due to Eddington-limited accretion (P. Podsiadlowski et al. 2003). Further examination shows that five of the initially viable cases (black dashed lines) are excluded because their post-CE orbital separations (Stage 4 in Figure 1) would cause the secondary to fill its Roche lobe prematurely. Consequently, only the two evolutionary tracks shown as red solid lines represent physically consistent solutions that simultaneously satisfy the observational constraints for GRO J1655.

Our complete simulation results[9] for GRO J1655, SAX J1819, and 4U 1543 are presented in Figures 4–6, respectively.

[9] We adopt a cutoff of $8.7\,M_\odot$ on the BH mass in our grid spaces for 4U 1543, as preliminary tests show that grids with higher BH masses are forbidden grids. When BH natal kicks are included, the allowable grids are further restricted to initial BH masses below $6.3\,M_\odot$ (see Figure 8). Thus, additional simulations with a more massive initial BH would not impact our conclusions. We also apply secondary mass cutoffs of $5.0\,M_\odot$ for GRO J1655 and $6.2\,M_\odot$ for SAX J1819, based on spectral observations, with detailed justification provided in Appendix A.

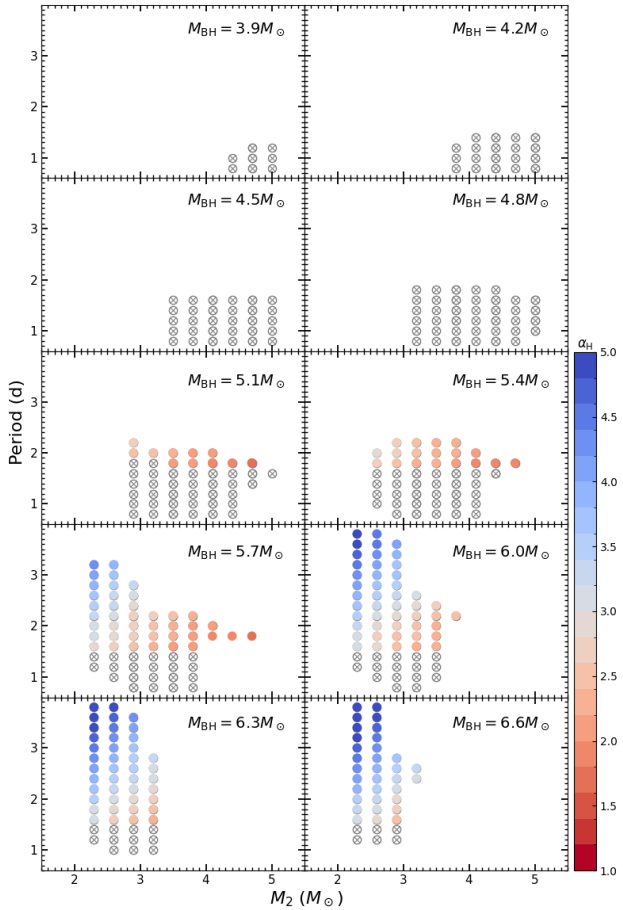

Figure 4. Parameter spaces for GRO J1655. All marked binaries can produce BHXBs consistent with GRO J1655's observed parameters. The viable parameter space consists of: colored solid circles, representing allowable solutions where post-CE separations (Stage 4) satisfy $R_2 < R_{2,\rm L}$, with the colors indicating $\alpha_{\rm H}$ values (assuming a $34\,M_\odot$ BH progenitor at $R_1 = 1000\,R_\odot$); and open circles, with crosses denoting forbidden grids violating this Roche lobe condition.

These figures distinguish between two distinct categories of evolutionary outcomes: (1) forbidden grid points (represented by black open circles with crosses) correspond to cases where the secondary star would prematurely fill its Roche lobe following CE ejection, analogous to the excluded black dashed trajectories in Figure 3; and (2) allowable grid points (shown as colored circles) successfully reproduce all observed parameters of the respective BHXB systems.

For each allowable grid point, we first obtain the binary parameters of the BH + MS binary at Stage 6 in Figure 1, then derive the corresponding He star + MS binary parameters at Stage 4. Using the known progenitor properties (including the envelope binding energy, core mass, and initial separation) for a given evolutionary stage, we calculate the required CE efficiency $\alpha_{\rm CE}$ by applying these parameters to Equation (1). The color bars in Figures 4–5 display the derived $\alpha_{\rm H}$ values for a representative $34\,M_\odot$ progenitor with radius $R = 1000\,R_\odot$. Notably, our analysis reveals: (1) no physically allowable solutions exist for 4U 1543 (Figure 6); (2) for GRO J1655 and SAX J1819, $\alpha_{\rm H}$ shows a positive correlation with $P_{\rm orb}$—i.e., wider initial orbits (Stage 6) require greater CE efficiencies to unbind the envelope; and (3) at fixed BH mass, $\alpha_{\rm H}$ decreases with increasing companion mass, as predicted by

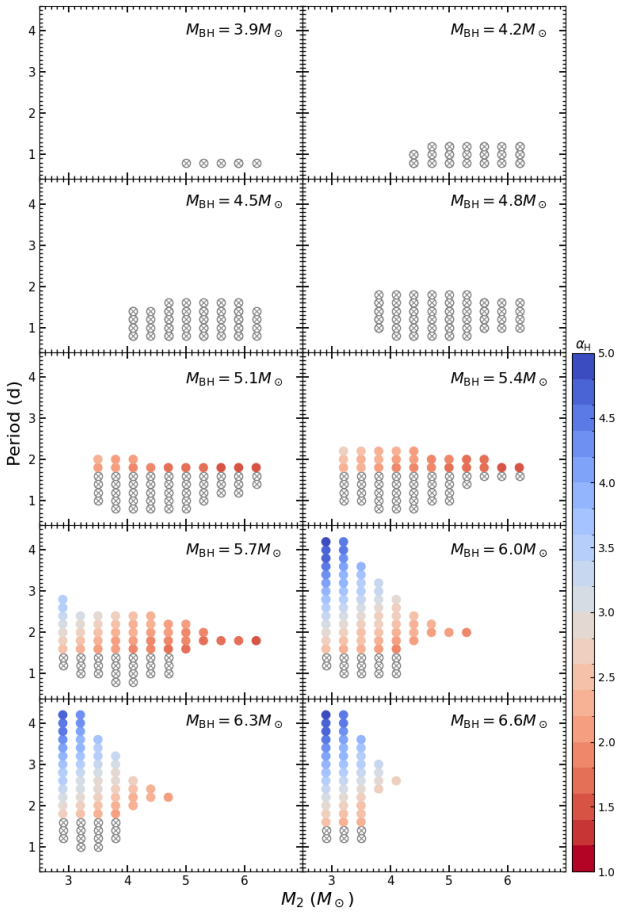

Figure 5. Similar to Figure 4 but for the parameter spaces of SAX J1819.

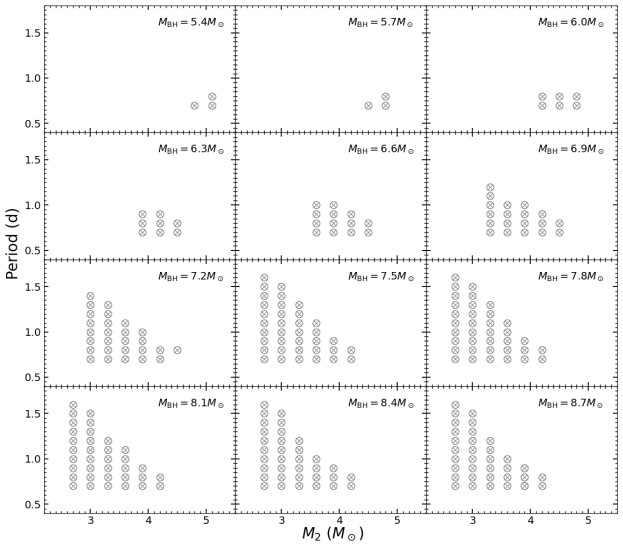

Figure 6. Similar to Figure 4 but for the parameter spaces of 4U 1543. Notably, no allowable parameter space exists for this system under the default zero-kick model.

Equation (1). These results assume zero BH natal kick; significant kick velocities would modify both the viable parameter space and derived CE efficiencies, as we explore in Section 3.2.

3.2. Effect of Kick

In our default model, we assume the BH forms with zero natal kick velocity. Under this assumption, the sudden mass loss during the SN explosion invariably widens the orbital separation (from Stage 5 to Stage 6 in Figure 1), allowing the post-CE binary separations to be directly derived from the parameter spaces shown in Figures 4–6. However, the scenario where BHs receive substantial natal kicks cannot be entirely ruled out, as suggested by observational evidence from some BH binaries (e.g., T. M. Tauris et al. 1999; S. Repetto & G. Nelemans 2015; F. Mirabel 2017; Y. Zhao et al. 2023; C. Dashwood Brown et al. 2024; Y. Abdulghani et al. 2025; A. Burrows et al. 2025; P. Nagarajan & K. El-Badry 2025). If a BH forms with a significant kick, the random orientation of the kick can either increase or decrease the orbital separation, thereby modifying the allowable parameter space to some degree, and consequently affecting the inferred CE efficiencies. In this section, we examine how BH natal kicks influence our previous results.

The modifications to the orbital parameters resulting from BH natal kicks are computed following the methodology of J. R. Hurley et al. (2002), as outlined below. We assume that the binary orbit is circular prior to BH formation (Stage 5 in Figure 1) and that the kick is instantaneously imparted to the newborn BH. Based on the Keplerian orbital equations and the principle of angular momentum conservation, the postkick semimajor axis a_n and eccentricity can be derived as follows:

$$\frac{1}{a_n} = \frac{2}{a_0} - \frac{GM_n}{V_n^2} \tag{10}$$

and

$$1 - e_n^2 = \frac{|\boldsymbol{r} \times \boldsymbol{V}_n|^2}{GM_n a_n}, \tag{11}$$

where the subscripts "0" and "n" denote the binary parameters before and after the kick, respectively ($M_n = M_{BH} + M_2$). The vector $\boldsymbol{V}_n$ represents the relative velocity after the kick ($V_n = |\boldsymbol{V}_n|$), which can be calculated by $\boldsymbol{V}_n = \boldsymbol{V}_{orb} + \boldsymbol{V}_K$, where $\overrightarrow{V_{orb}}$ is the pre-SN orbital velocity. $\overrightarrow{r}$ is the initial separation vector between the two stars. In this study, we adopt the simplifying assumption that the kick direction is randomly distributed. Thus, for a given kick speed V_K, the postkick orbital parameters can be determined using Equations (10)–(11).

3.2.1. Formation of 4U 1543 with a Natal Kick

As discussed above, no viable parameter space exists for the formation of 4U 1543 if the BH forms with zero natal kick velocity. This is because the orbital separations at Stage 4 for binaries within the parameter space of Figure 6 are sufficiently small that the MS companions would fill their Roche lobes, preventing the system from evolving into an X-ray binary. However, if the BH receives a natal kick, the post-SN orbital separation may decrease, depending on the kick direction. To examine this scenario, we adopt a BH progenitor of $34\,M_\odot$ undergoing CE evolution at $1000\,R_\odot$ (the initial parameter choices affect only the CE efficiency estimates without impacting our conclusions). We define a minimum separation a_{min} at Stage 4, where the MS star just fills its Roche lobe post-CE, determined by the secondary's mass and radius. For a given kick velocity and each grid point in Figure 6, we

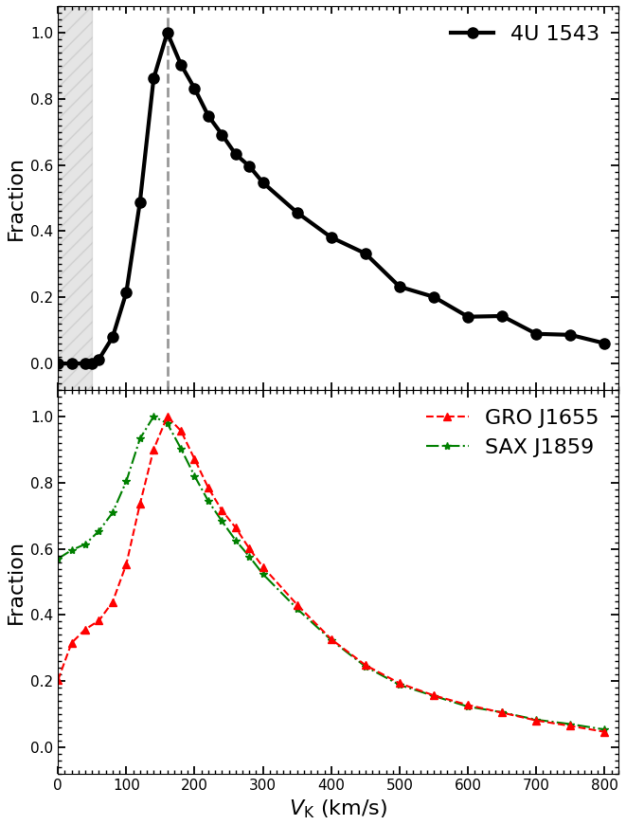

Figure 7. Upper panel: the fraction of the sampled binary systems that successfully evolve into the parameter space corresponding to 4U 1543. Lower panel: similar to the upper panel, but for GRO J1655 (red dashed line) and SAX J1819 (green dashed–dotted line). For a given kick velocity, we randomly generate 10^5 He star + MS binaries with varying orbital separations (Stage 4 in Figure 1), and count systems that subsequently fall within the target parameter space. The resulting fractions are normalized to their peak value. The hatched region in the upper panel indicates kick velocities ($V_K \leqslant 50$ km s^{-1}) for which no binary systems can fall within the parameter spaces in Figure 6, representing the minimum kick velocity required for the formation of 4U 1543.

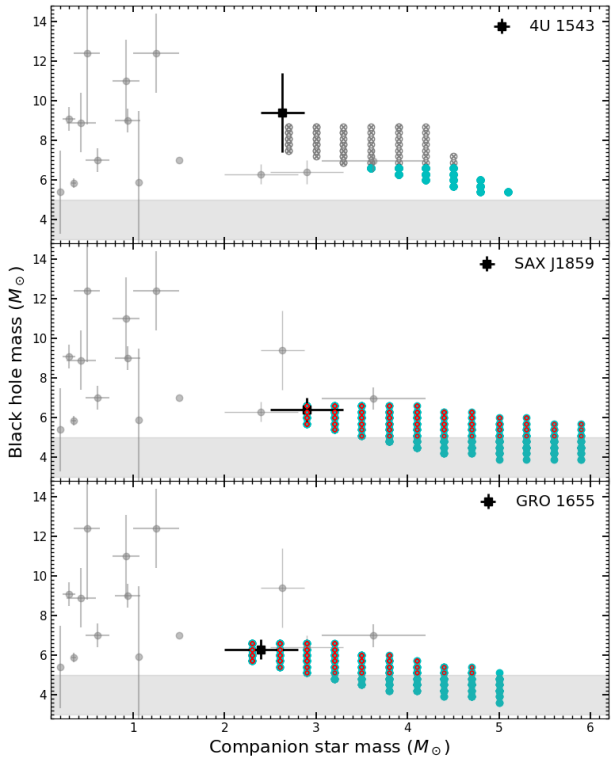

Figure 8. The BH mass and companion star mass distributions for the grid points shown in Figures 4–6. The upper panel distinguishes between the forbidden configurations (gray open circles with crosses) and viable systems when BH natal kicks are included (cyan circles). The middle and lower panels display the allowable parameter space for systems excluding (red open circles) and including (cyan circles) BH natal kicks, respectively. The observed BHXB samples are taken from J. M. Corral-Santana et al. (2016).

generate 10^5 binaries with the orbital separations at Stage 4 distributed logarithmically between $a_{\rm min}$ and $10a_{\rm min}$. Finally, we count systems that successfully evolve into 4U 1543–like BHXBs, assuming uniform probability per grid point.

The statistical results, normalized to their peak value, are shown in the upper panel of Figure 7. Our analysis reveals that for kick velocities $V_K \leqslant 50$ km s^{-1}, no binary systems fall within the parameter space required for 4U 1543 formation as shown in Figure 6. This strongly suggests that if 4U 1543 formed through isolated binary evolution, its BH must have received a natal kick of at least 50 km s^{-1}. We identify a preferred kick velocity of $V_K = 160$ km s^{-1}, which maximizes the probability of forming 4U 1543–like BHXBs. Furthermore, the formation probability becomes significantly reduced for systems with extremely high kick velocities ($V_K \gtrsim 800$ km s^{-1}). For comparison, we also calculated the corresponding results for GRO J1655 and SAX J1819, which are shown in the lower panel. Similarly, the preferred kick velocity that maximizes the formation probability for GRO J1655–like/SAX J1819–like BHXBs is about 140–160 km s^{-1}. We note, however, that the above conclusions should be interpreted with caution, owing to the small sample size of observed BHXBs and the incomplete understanding of the physical mechanisms governing natal kicks.

3.2.2. Influence of Kick on BH Birth Mass

The influence of BH natal kicks extends beyond 4U 1543, to affect the parameter spaces of SAX J1819 and GRO J1655 as well. Figure 8 displays the BH mass and companion star mass distributions corresponding to the grid points in Figures 4–6. The upper panel distinguishes between forbidden grids (gray open circles with crosses) and viable systems when BH kicks are considered (cyan circles). The middle and lower panels compare systems without BH kicks (red open circles, representing the allowable grids from Figures 4 and 5) to those with kicks. Notably, BH natal kicks significantly expand the allowable parameter space. Most remarkably, for both SAX J1819 and GRO J1655, the inclusion of natal kicks allows for BH formation in the so-called mass-gap region $\sim 3-5\,M_\odot$ (Y. Shao 2022; S. Wang et al. 2024)—a scenario prohibited in the zero-kick case.

3.2.3. Influence of Kick Velocity on CE Efficiency

As discussed above, when accounting for nonzero BH kick velocities, the binary separation at Stage 4 cannot be determined directly from Equations (5)–(7). To address this, we implement a Monte Carlo approach to systematically evaluate how kick velocities influence CE efficiency. We first select representative grid points from Figure 4 (for GRO

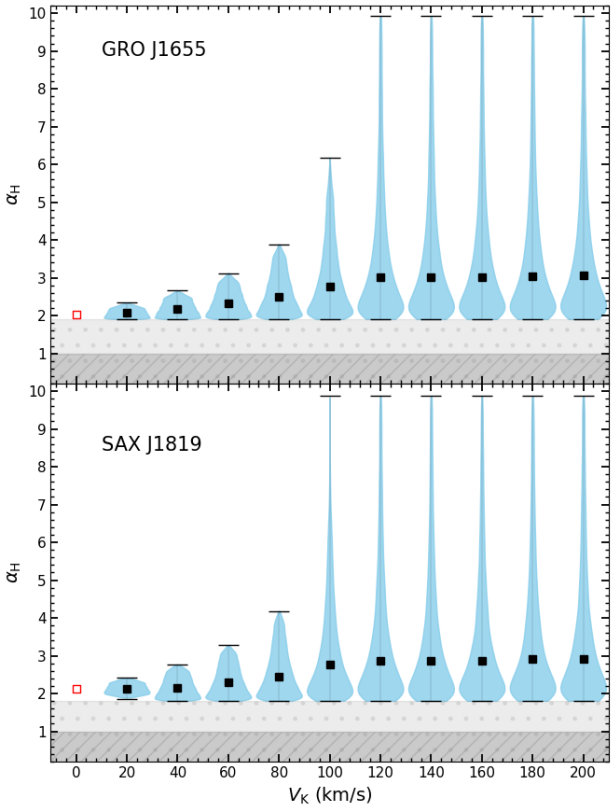

Figure 9. The influence of the kick velocity on the CE efficiency (α_H). The chosen grid points for GRO J1655 and SAX J1819 are $M_{BH} = 5.1$, $M_2 = 4.1\,M_\odot$, $P_{orb} = 2.0$ days and $M_{BH} = 5.7$, $M_{2,i} = 4.4\,M_\odot$, $P_{orb} = 2.0$ days, respectively. The BH progenitor is assumed to have an initial mass of $32\,M_\odot$ with the CE occurring when the progenitor reaches a stellar radius of $1000\,R_\odot$. For the zero-kick case, the corresponding α_H values are shown by the red open squares. The distribution of α_H values is illustrated in the violin plot, where the median values are represented by black squares. A cutoff of $\alpha_H = 10$ is applied for systems with large kick velocities. The light gray hatched regions denote cases where the post-CE orbital separation falls below the minimum threshold a_{min}, while the dark gray hatched regions indicate scenarios with $\alpha_H < 1$.

J1655) and Figure 5 (for SAX J1819), each defining the minimum allowable separation a_{min} at Stage 4. For each grid point, we generate 10^6 binary systems with orbital separations log-uniformly distributed across (a_{min}, $10a_{min}$), then apply the SN kick and track whether the post-SN parameters fall within the original grid point. The fraction of systems remaining within the grid boundaries serves as a statistical weight for the corresponding CE efficiency calculated via Equation (1).

Figure 9 demonstrates the impact of the kick velocity on the CE efficiency parameter α_H for selected systems: GRO J16550 ($M_{BH} = 5.1\,M_\odot$, $M_2 = 4.1\,M_\odot$, $P_{orb} = 2.0$ days) and SAX J1819 ($M_{BH} = 5.7\,M_\odot$, $M_2 = 4.4\,M_\odot$, $P_{orb} = 2.0$ days), both originating from a $32\,M_\odot$ progenitor undergoing CE evolution at $R = 1000\,R_\odot$. The zero-kick case (red open squares) is also shown for comparison. Our Monte Carlo results are presented by violin plots with median values (black squares). The light gray hatched regions indicate systems where the post-CE separation falls below a_{min}, while the dark gray regions correspond to cases with $\alpha_H < 1$. Our results show that while the estimated CE efficiencies for systems with kicks may be slightly lower than those in the zero-kick case, the median α_H values exhibit a gradual increase with higher BH kick velocities. Most significantly, even when accounting for BH kicks, all α_H values remain greater than 1 (mainly because of the limitation of a_{min}).

3.3. Progenitor Mass Dependence of Minimum α_{CE}

The CE efficiency parameter α_{CE} is primarily determined by three key factors: (1) the initial primary mass (BH progenitor), which sets the stellar structure; (2) the evolutionary stage at CE onset, which affects the envelope binding energy E_{bind}; and (3) the post-CE binary parameters that govern the orbital energy release. For each allowable grid point (4U 1543 can also have allowable grid points when accounting for significant BH kick velocities; see Figure 8) in our parameter space, we compute the CE efficiency for fixed BH progenitor masses at specific evolutionary stages (characterized by stellar radii), enabling us to determine the minimum required α_{CE} values as functions of initial primary mass and evolutionary stage, as shown in Figure 10 (GRO J1655), Figure 11 (SAX J1819), and Figure 12 (4U 1543). It should be noted that the minimum CE efficiency is primarily governed by the threshold binary separation (a_{min}), a quantity unaffected by BH natal kicks. Here, we present the results only for BH progenitors with masses of $32-40\,M_\odot$; the corresponding results for more massive BH progenitors can be found in Appendix B.

We see that the minimum CE efficiency does not always increase monotonically with the mass of the BH progenitor when other parameters are held fixed. This behavior can be understood as follows. For a BH progenitor filling its Roche lobe at a given evolutionary stage, a more massive progenitor typically produces a more massive He star after CE ejection. According to Equations (5)–(7), a more massive He star tends to result in a wider post-BH-formation orbit. Inversely, for a specific grid point in the parameter space, a more massive progenitor would lead to a shorter post-CE orbital separation. Consequently, although a more massive BH progenitor generally has a larger envelope binding energy, the shorter post-CE separation can yield a lower estimated CE efficiency (according to Equation (1)). Furthermore, the allowable parameter space varies with the initial BH progenitor mass, which affects the derived minimum CE efficiency values. This dependence explains why the $33\,M_\odot$ progenitor exhibits relatively lower minimum CE efficiency compared to the $32\,M_\odot$ case when both systems are undergoing CE evolution at similar evolutionary stages.

When enthalpy is not considered (the left and middle panels of Figures 10–12), the envelope becomes progressively easier to eject at later evolutionary stages, due to the decreasing binding energy as the star expands (Figure 2). In contrast, when enthalpy is included (the right panels), the derived α_H values exhibit only modest variations for a given BH progenitor, reflecting the weak dependence of the binding energy on stellar radius (Figure 2). The derived CE efficiency constraints are:

1. GRO J1655: $\alpha_{0.5U} \gtrsim 7-9$, $\alpha_U \gtrsim 4-6$, $\alpha_H \gtrsim 1.7$;
2. SAX J1819: $\alpha_{0.5U} \gtrsim 5-8$, $\alpha_U \gtrsim 3-5$, $\alpha_H \gtrsim 1.4$; and
3. 4U 1543: $\alpha_{0.5U} \gtrsim 5.5-9$, $\alpha_U \gtrsim 3.5-5$, $\alpha_H \gtrsim 1.6$.

Notably, all three efficiency values exceed unity across these systems.

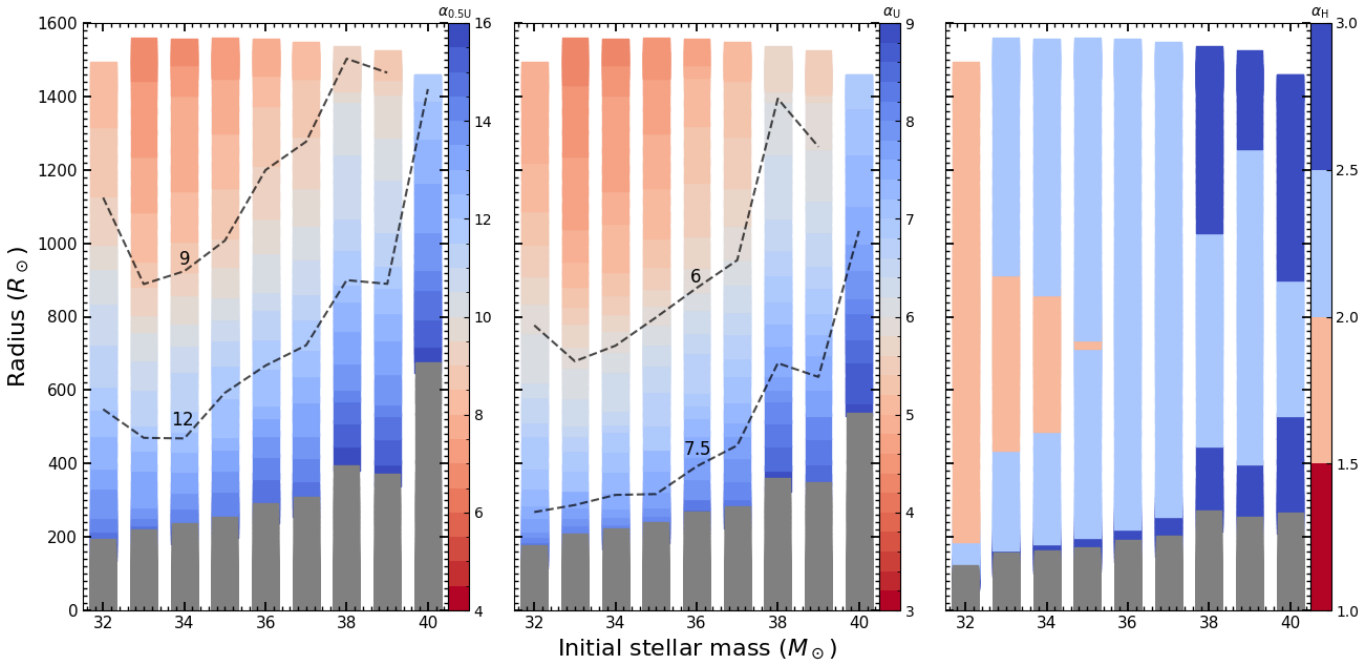

Figure 10. The minimum values of CE efficiency for GRO J1655 vary with the initial primary mass and the stellar radius. The left, middle, and right panels correspond to the $\alpha_{0.5U}$, α_U, and α_H cases, respectively. The shaded gray region indicates CE efficiencies above the upper limit of the color bar. The dashed lines indicate constant minimum CE efficiency values. Notably, when enthalpy is included (right panel), the minimum CE efficiencies show significantly less variation, typically confined to a narrow range of 1.5−3.

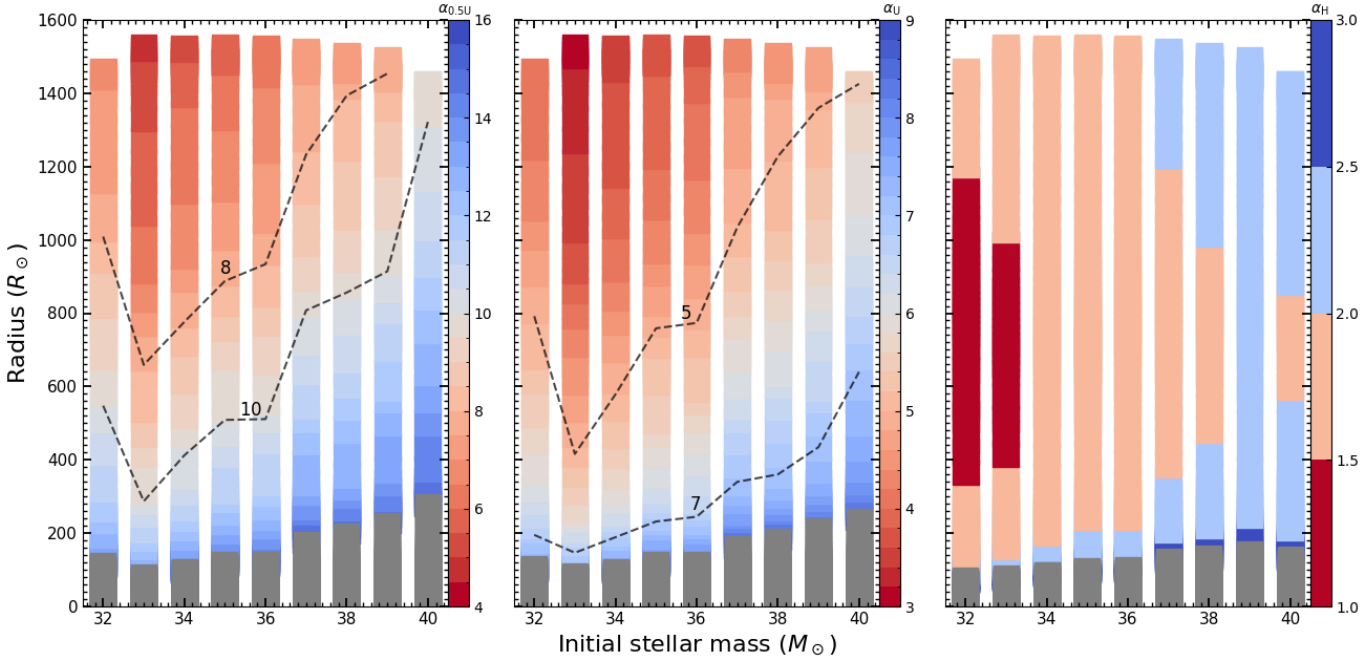

Figure 11. Similar to Figure 10 but for the case of SAX J1819.

3.4. Suggested α_{CE} Lower Limit

Our results demonstrate that multiple factors significantly influence the estimation of CE efficiencies, including the binary progenitor masses, the evolutionary stage of the BH progenitor at CE initiation, and BH natal kicks. Given the substantial uncertainties in these parameters, precise constraints on CE efficiency ranges remain challenging. However, we can establish well-defined lower limits for these efficiencies. Figure 13 presents the minimum CE efficiencies α_H, α_U, and $\alpha_{0.5U}$ for all three studied BHXBs, determined by their respective a_{min} values, which are unaffected by BH kicks. The dependence of the minimum CE efficiency on the initial BH progenitor mass is shown in Figure 18 (Appendix C). Crucially, none of the systems permit solutions with CE efficiencies below unity. To

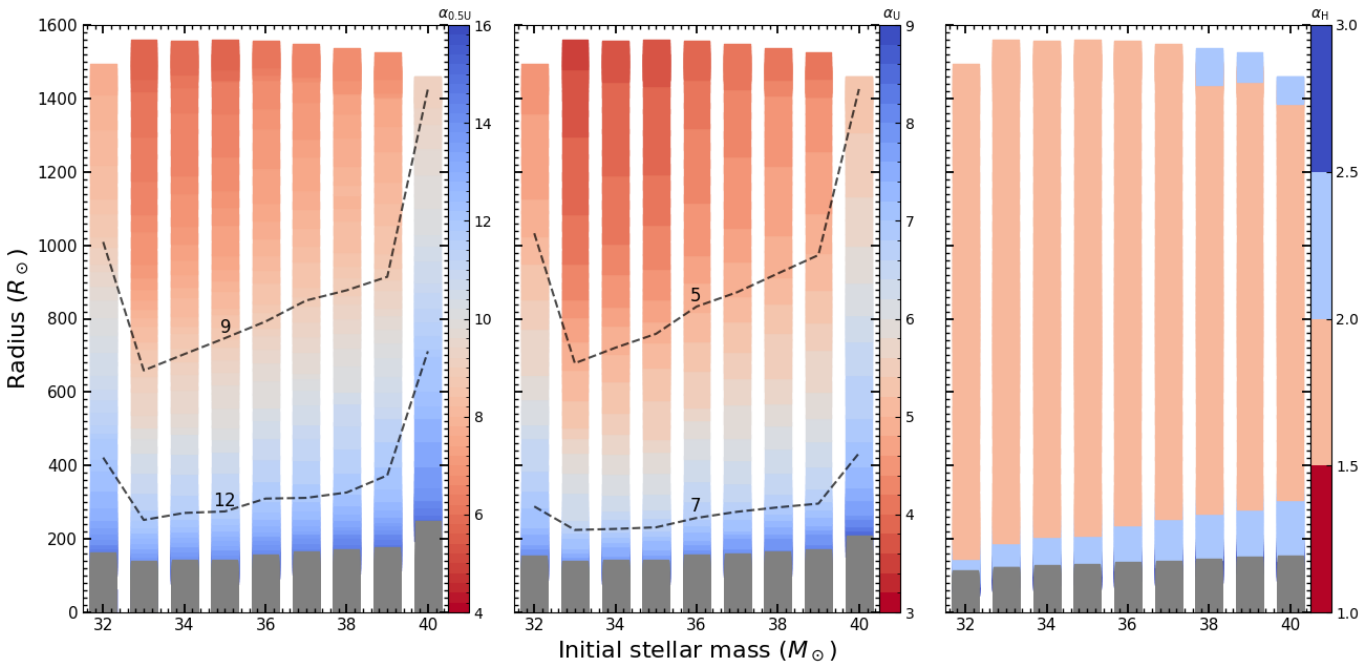

Figure 12. Similar to Figure 10 but for the case of 4U 1543, where the minimum CE efficiency values are calculated using the critical orbital separation $a_{\rm min}$ at Stage 4.

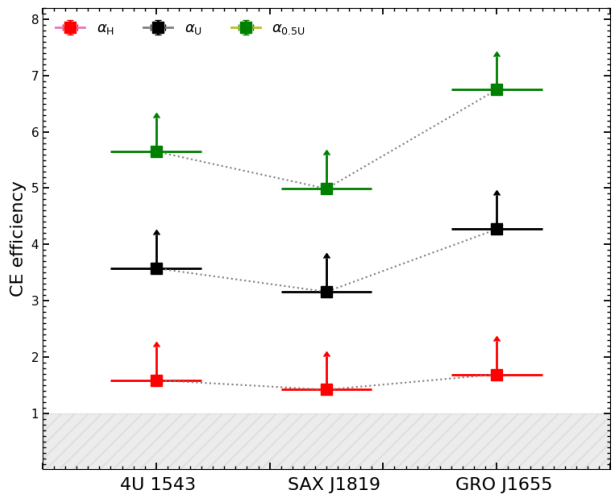

Figure 13. The minimum CE efficiencies required to form the three BHXBs. The red, black, and green symbols correspond to the values of $\alpha_{\rm H}$, $\alpha_{\rm U}$, and $\alpha_{0.5{\rm U}}$, respectively. To simultaneously explain the formation of all three BHXBs, higher efficiency thresholds are required: $\alpha_{0.5{\rm U}} \gtrsim 6.7$, $\alpha_{\rm U} \gtrsim 4.2$, and $\alpha_{\rm H} \gtrsim 1.7$.

simultaneously explain the formation of all three BHXBs, we require significantly higher efficiency thresholds: $\alpha_{0.5{\rm U}} \gtrsim 6.7$, $\alpha_{\rm U} \gtrsim 4.2$, and $\alpha_{\rm H} \gtrsim 1.7$. These findings strongly suggest that successful CE ejection in massive binaries necessitates high efficiency parameters, in agreement with previous studies of massive binary evolution (P. Podsiadlowski et al. 2003; T. Fragos et al. 2019; M. Mapelli et al. 2026).

4. Discussion

In this study, we have constrained the CE phase in massive binary systems through analysis of three observed BHXBs. Using the standard energy formalism for CE ejection, we have determined robust lower limits for the CE efficiency parameters. Specifically, all three systems require CE efficiencies greater than unity $\alpha_{\rm CE} > 1$, even when accounting for enthalpy contributions that substantially reduce the envelope binding energy. This strongly suggests that either additional energy sources are required within the energy formalism of the commonly adopted CE description or, alternatively, the description itself needs to be modified. We now proceed to discuss our results in more detail.

1. *Core–Envelope Boundary*. One of the largest uncertainties in calculating the envelope binding energy lies in the definition of the core–envelope boundary. In this work, we adopt a physically motivated prescription, where the boundary is determined by the maximum compression point (N. Ivanova 2011). Under this assumption, the core–envelope boundary typically corresponds to a hydrogen mass fraction of $X_{\rm H} \approx 0.1$–0.3. This adopted boundary is located farther out (i.e., closer to the stellar surface) compared to the commonly used criterion in binary population synthesis studies, which often take $X_{\rm H} = 0.1$ as the core–envelope boundary (e.g., M. U. Kruckow et al. 2016, 2018). Moving the boundary outward would undoubtedly reduce the envelope binding energy and thus lower the inferred $\alpha_{\rm CE}$ values. However, a more outward boundary also implies that more hydrogen remains in the envelope, which may lead to the significant re-expansion of the stripped core after the CE phase (e.g., O. De Marco et al. 2011; P. Marchant et al. 2021; A. Vigna-Gómez et al. 2022). Recent simulations by A. Vigna-Gómez et al. (2022) examined the stellar response following the removal of the hydrogen-rich envelope. They found that the boundary allowing the star to avoid rapid re-expansion lies above the maximum compression point. Nevertheless, their simulations focused on stars with masses below $25\,M_\odot$, while our work primarily targets more massive stars ($\geqslant 32\,M_\odot$). This mass difference may result in different

poststripping behavior. A key distinction is that for stars below $25\,M_{\odot}$, the maximum compression point is generally located at $X_{\rm H} < 0.1$ (A. Vigna-Gómez et al. 2022). In contrast, for stars with masses $\gtrsim 32\,M_{\odot}$, we find that the maximum compression point falls in the range $0.1 < X_{\rm H} < 0.3$. Therefore, both the appropriate definition of the core–envelope boundary and the post-CE evolution of the stripped core remain open questions that warrant further investigation.

2. *Extra Energy Sources—Nuclear Energy*. P. Podsiadlowski et al. (2010) suggested that nuclear energy could contribute to envelope ejection. In this scenario, hydrogen-rich material from the low-mass companion is injected into the helium-burning shell of the massive donor during the late CE phase, triggering a nuclear runaway that explosively ejects both the hydrogen and helium layers. The result is a close binary containing a compact object and a low-mass companion. This channel is, however, very rare and requires the low-mass companion to overflow its Roche lobe during the self-regulated spiral-in phase, to transfer hydrogen-rich material deep into the donor's helium shell (see also N. Ivanova 2002; N. Ivanova et al. 2020). This channel involves complex mass-transfer processes within the CE that are difficult to model with current simulations, and it therefore remains a topic for future work.
3. *Extra Energy Sources—Jets*. The possibility that jets launched from the accreting companion serve as an additional energy source during CE evolution has gained substantial support from recent theoretical, numerical, and observational studies. Numerical simulations have demonstrated that jets can remove mass before and during the CE phase, reduce drag forces, and facilitate envelope unbinding (e.g., N. Soker 2004, 2015; S. Shiber & R. Iaconi 2024; Y. Weiner & N. Soker 2025). Furthermore, the newly proposed jetted mass-removal accretion mechanism indicates that MS stars can accrete at high rates, provided that jets remove the outer high-entropy layers of the accreted envelope (E. Bear & N. Soker 2025; A. Scolnic et al. 2025; Y. Cohen et al. 2026; but see also Y. Zou et al. 2022). Observationally, jets appear to be the most robust observable ingredient of CE evolution, found in about 40% more post-CE planetary nebulae than dense equatorial outflows (N. Soker 2025). Collectively, these developments suggest that jets may be regarded as a primary candidate for the missing energy source in CE evolution. However, quantitative simulations are still needed to accurately determine the contribution of jets to the envelope unbinding during the CE phase.
4. *Tidal Effects*. Tidal interactions could indirectly influence the estimated CE efficiency. If sufficiently strong, tides can significantly tighten the orbital separation as the massive star evolves into a red supergiant (RSG). In this scenario, the donor star may not initially fill its Roche lobe at its maximum radial extent, enabling continuous mass loss during the RSG phase, as tides gradually shrink the orbit. By the onset of the CE phase (when the star finally fills its Roche lobe), a substantial portion of the envelope may have already been lost. This process is quite similar to the grazing envelope evolution proposed by N. Soker (2015), in which jets remove some envelope mass before the CE phase (see also S. Shiber & R. Iaconi 2024), thereby substantially reducing the binding energy (I. Kotko et al. 2024). However, it is important to emphasize that current tidal theory still contains significant uncertainties, particularly regarding the efficiency of orbital decay (e.g., S. Meibom & R. D. Mathieu 2005; G. I. Ogilvie 2014; J. D. Nie et al. 2017).
5. *Modified Energy Mechanism*. In the standard energy formalism adopted in this work, the envelope's energy profile is assumed to remain constant during CE ejection. However, recent studies (P. Marchant et al. 2021; H. Ge et al. 2022, 2024b) have proposed that the donor star's structure may evolve significantly, due to rapid mass loss during the CE phase. In particular, H. Ge et al. (2022) developed a self-consistent approach to calculate the envelope's binding energy, by treating the total energy as a function of the remnant mass. Preliminary results suggest that the CE efficiency need not be constant, but a function of the initial mass ratio (H. Ge et al. 2024b). Further investigation is required to determine whether this modified framework can consistently explain the formation of BHXBs with $\alpha_{\rm CE} < 1$ while maintaining physical self-consistency.
6. *Alternative CE Description*. Recent work by R. Hirai & I. Mandel (2022) has proposed a novel two-stage CE ejection mechanism for massive binaries, motivated by the stellar structure of RSGs that typically exhibit a substantial radiative layer between their dense He cores and outer convective envelopes. In this model, CE evolution proceeds through distinct phases—i.e., rapid inspiral through the convective envelope, followed by stable mass transfer from the radiative intershell region (see also P. Marchant et al. 2021; M. Gallegos-Garcia et al. 2023; Y.-D. Nie et al. 2025). Given that the later phase involves stable mass transfer between the core (radiative intershell region) and the companion, the final post-CE separation is determined by the angular momentum loss mechanism and the specific binary parameters prevailing during the mass-transfer epoch. However, recent simulations by T. Cohen & N. Soker (2023) suggested that the inner boundary of the envelope convective zone moves deep into the initial radiative zone, highlighting the uncertainties inherent in this formalism. Apart from the energy-based CE prescription, the γ-mechanism (e.g., G. Nelemans et al. 2000; G. Nelemans & C. A. Tout 2005; R. Di Stefano et al. 2023) treats the CE phase via angular momentum conservation. Although the γ-mechanism appears to reproduce some observed binary systems better than the energy formalism (e.g., G. Nelemans et al. 2025), the underlying physical picture remains unclear.
7. *Alternative Formation Channels*. Given that significant uncertainties remain in explaining BHXB formation through isolated binary evolution, several studies have proposed alternative pathways, including dynamical interactions in dense stellar environments and three-body systems (P. P. Eggleton & F. Verbunt 1986; S. Naoz et al. 2016; J. Klencki et al. 2017; C. Shariat et al. 2025). These alternative channels are physically viable, but rigorous validation through detailed *N*-body

simulations and comparison with increasingly larger BHXB samples are still required.

Clearly, our current understanding of BHXB formation mechanisms remains incomplete, with several fundamental questions still open.

5. Conclusions

This work establishes critical lower limits for CE efficiency parameters ($\alpha_{0.5U}$, α_{U}, α_{H}) during massive binary evolution, providing essential benchmarks for population synthesis studies. When accounting solely for internal energy contributions, we find minimum required efficiencies of $\alpha_{0.5U} \gtrsim 6.7$ and $\alpha_{U} \gtrsim 4.2$ for successful envelope ejection. Notably, including enthalpy, which substantially reduces the envelope binding energy, lowers this threshold to $\alpha_{H} \gtrsim 1.7$, though all values significantly exceed unity, suggesting that additional energy sources (such as jets) may be necessary. Alternatively, this may indicate that the current description of the CE phase needs to be revised.

BH natal kicks remain one of the most critical uncertainties in BH formation scenarios. Our analysis reveals that 4U 1543 cannot form through isolated binary evolution with kick velocities below $\sim$50 km s^{-1}, with a preferred formation probability peak at 160 km s^{-1}. We also systematically investigate how BH natal kicks influence CE efficiency and find that: (1) typical α_{CE} values increase with higher kick velocities; and (2) all viable solutions maintain $\alpha_{CE} > 1$ regardless of kick magnitude.

A growing consensus suggests that classical energy mechanisms, which we define here as those relying solely on orbital energy and internal or recombination energy and excluding external sources such as jets, fail to provide sufficient energy for CE ejection in massive binaries, as supported by the systematic need for $\alpha_{CE} > 1$ in population synthesis models attempting to match the observed properties of post-CE massive binaries (P. D. Kiel & J. R. Hurley 2006; L. R. Yungelson et al. 2006; A. Grichener 2023). Our results confirm that while the classical energy formalism offers simplicity and computational convenience, it faces fundamental limitations in describing massive binary CE evolution. These findings highlight the critical need to either modify existing CE prescriptions or develop new theoretical frameworks that properly incorporate the complex physics of massive envelope ejection.

Acknowledgments

We deeply thank the referee for a very careful reading and constructive comments that have led to the improvement of the manuscript. The authors are grateful to Poshak Gandhi for his valuable suggestions and feedback on this work. This work is supported by the Natural Science Foundation of China (grant Nos. 12125303, 12525304, 12288102, 12473034, 12103028, 12333008, 12422305, 12090040/3, 12273105, 11703081, 11422324, 12073070, and 12173081), the CAS Project for Young Scientists in Basic Research (YSBR-148), the Strategic Priority Research Program of the Chinese Academy of Sciences (grant Nos. XDB1160303, XDB1160201, and XDB1160000), the National Key R&D Program of China (grant Nos. 2021YFA1600403 and 2021YFA1600400), the Key Research Program of Frontier Sciences of CAS (No. ZDBS-LY-7005), the "CAS Light of West China", the Yunnan Revitalization Talent Support Program-Science & Technology Champion Project (No. 202305AB350003) and Young Talent Project, the International Centre of Supernovae (ICESUN), Yunnan Key Laboratory of Supernova Research (Nos. 202302AN360001 and 202201BC070003), Yunnan Fundamental Research Projects (No. 202401AT070139), and the Natural Science Foundation of Henan Province (No. 242300420944). X.C. acknowledges the New Cornerstone Science Foundation through the XPLORER PRIZE. The authors gratefully acknowledge the "PHOENIX Supercomputing Platform" jointly operated by the Binary Population Synthesis Group and the Stellar Astrophysics Group at Yunnan Observatories, Chinese Academy of Sciences.

Software: MESA (v.12115; B. Paxton et al. 2011, 2013, 2015, 2018, 2019; A. S. Jermyn et al. 2023).

Example MESA inlists that we used to generate our models are archived on Zenodo and can be downloaded via doi:10.5281/zenodo.19660373.

Appendix A
The Cutoff of the Secondary Mass

We establish secondary mass cutoffs for GRO J1655 and SAX J1819 based on spectral observations of their companion stars. Figure 14 presents the evolutionary tracks for both systems (GRO J1655 in the left panels and SAX J1819 in the right panels) as functions of secondary mass, which constrain the upper mass limits of these companions. For GRO J1655, we impose a 5.0 $M_{\odot}$ cutoff, because more massive companions cannot match the system's observed effective temperature. Similarly, for SAX J1819.8-2523, we adopt a 6.2 $M_{\odot}$ cutoff, since more massive companions exceed the system's observed parameter space.

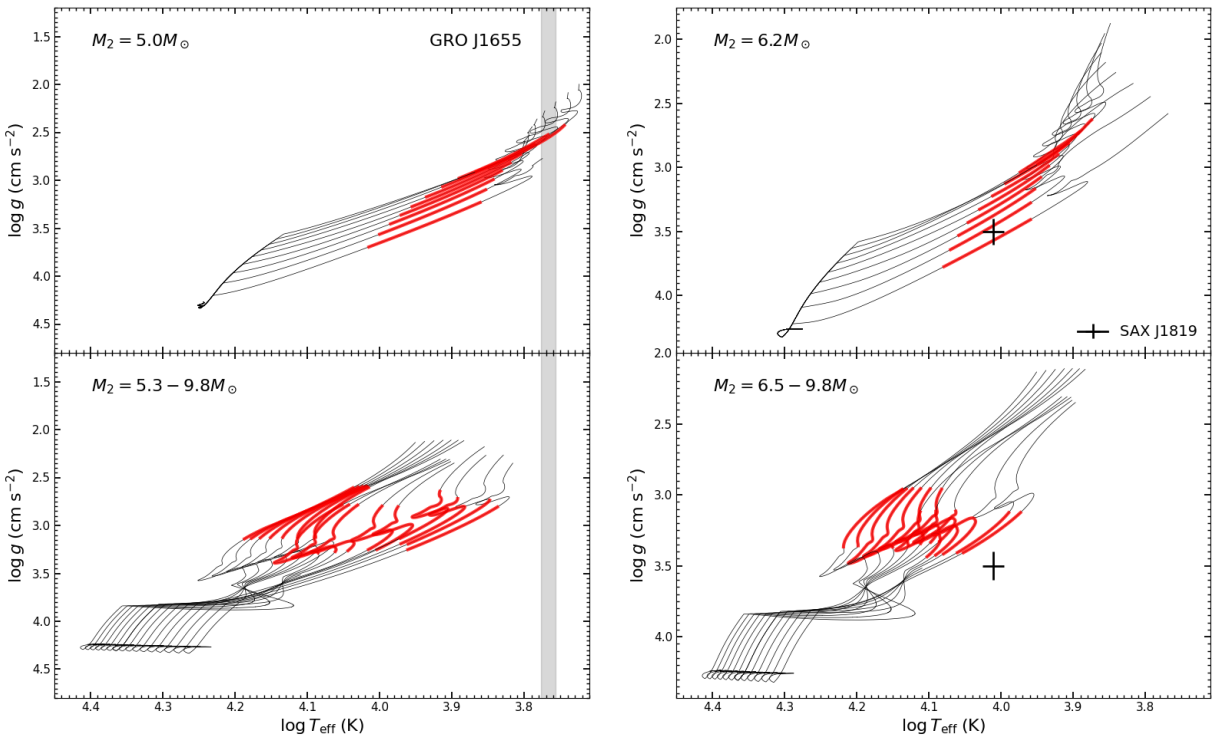

Figure 14. The evolutionary tracks for GRO J1655 (left panels) and SAX J1819 (right panels) as functions of varying secondary masses, which are used to constrain the upper mass limits of the secondary stars. For GRO J1655, we adopt a mass cutoff of 5.0 $M_\odot$, beyond which more massive secondaries cannot reproduce the observed effective temperature of the system. Similarly, for SAX J1819, we implement a cutoff at 6.2 $M_\odot$, as more massive secondaries generally evolve beyond the observed parameter space of this system. The red solid lines indicate cases where the secondary masses fall within the observed ranges for each binary.

Appendix B
The CE Efficiencies with More Massive BH Progenitors

In Figures 15–17, we present the minimum CE efficiency requirements for GRO J1655, SAX J1819, and 4U 1543, respectively, considering more massive BH progenitors. The results suggest systematically higher CE efficiency values compared to systems with lower-mass BH progenitors.

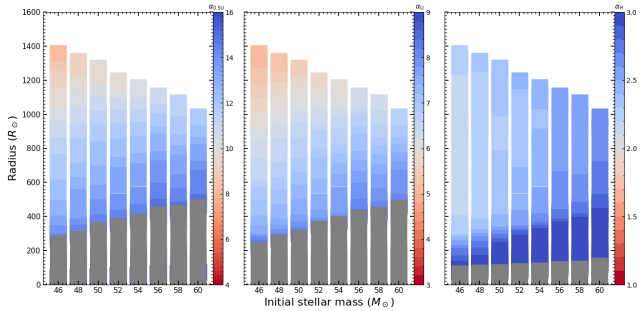

Figure 15. The minimum CE efficiency requirements in the cases of 46−60 $M_\odot$ BH progenitors for GRO J1655.

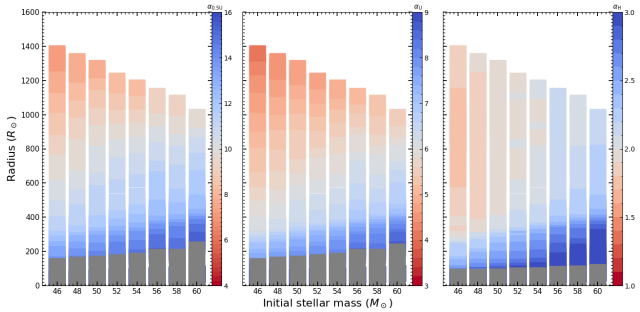

Figure 16. The minimum CE efficiency requirements in the cases of 46−60 $M_\odot$ BH progenitors for SAX J1819.

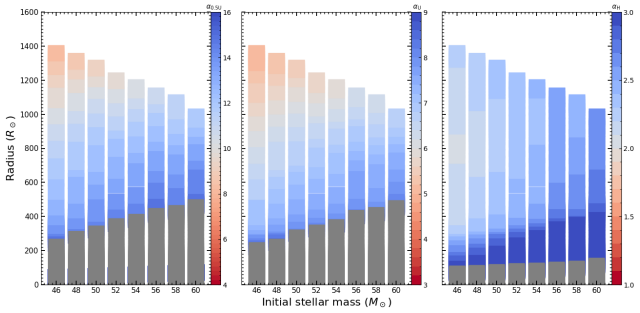

Figure 17. The minimum CE efficiency requirements in the cases of 46 −60 $M_\odot$ BH progenitors for 4U 1543.

Appendix C
Minimum CE Efficiencies as Functions of BH Progenitor Masses

Figure 18 presents the minimum CE efficiencies as functions of initial BH progenitor masses for the three BHXBs. The open squares denote the corresponding minimum CE efficiency values previously shown in Figure 13.

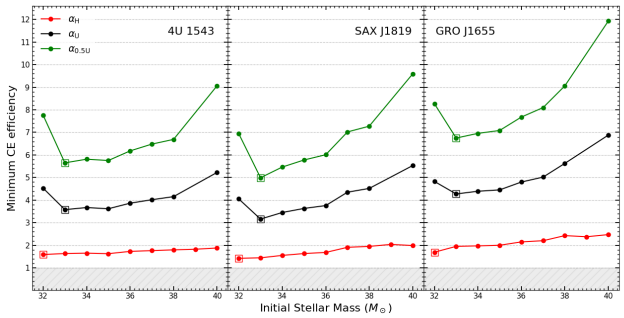

Figure 18. Minimum CE efficiencies as functions of initial BH progenitor masses for the three BHXBs. The open squares denote the corresponding minimum CE efficiency values previously shown in Figure 13.

ORCID iDs

Zhenwei Li https://orcid.org/0000-0002-1421-4427
Dandan Wei https://orcid.org/0000-0003-0821-4583
Shi Jia https://orcid.org/0000-0001-6808-638X
Hailiang Chen https://orcid.org/0009-0006-9211-2860
Hongwei Ge https://orcid.org/0000-0002-6398-0195
Zhuo Chen https://orcid.org/0000-0001-7420-9606
Yangyang Zhang https://orcid.org/0009-0008-3363-265X
Xuefei Chen https://orcid.org/0000-0001-5284-8001
Zhanwen Han https://orcid.org/0000-0001-9204-7778

References

Abdulghani, Y., Lohfink, A. M., & Chauhan, J. 2025, MNRAS, 541, 553
Aguilera-Dena, D. R., Müller, B., Antoniadis, J., et al. 2023, A&A, 671, A134
Asplund, M., Grevesse, N., Sauval, A. J., & Scott, P. 2009, ARA&A, 47, 481
Bear, E., & Soker, N. 2025, RAA, 25, 025010
Beer, M. E., & Podsiadlowski, P. 2002, MNRAS, 331, 351
Belloni, D., & Schreiber, M. R. 2023, in Handbook of X-Ray and Gamma-Ray Astrophysics, ed. C. Bambi & A. Santangelo (Springer), 129
Belloni, D., Schreiber, M. R., & Zorotovic, M. 2024a, A&A, 687, A12
Belloni, D., Zorotovic, M., Schreiber, M. R., et al. 2024b, A&A, 686, A61
Blaauw, A. 1961, BAN, 15, 265
Boersma, J. 1961, BAN, 15, 291
Briel, M. M., Stevance, H. F., & Eldridge, J. J. 2023, MNRAS, 520, 5724
Bronner, V. A., Schneider, F. R. N., Podsiadlowski, P., & Röpke, F. K. 2024, A&A, 683, A65
Burrows, A., Wang, T., & Vartanyan, D. 2025, ApJ, 987, 164
Chamandy, L., Frank, A., Blackman, E. G., et al. 2018, MNRAS, 480, 1898
Chen, W.-C., & Li, X.-D. 2006, MNRAS, 373, 305
Chen, X., Liu, Z., & Han, Z. 2024, PrPNP, 134, 104083
Choi, J., Dotter, A., Conroy, C., et al. 2016, ApJ, 823, 102
Cohen, T., & Soker, N. 2023, RAA, 23, 065023
Cohen, Y., Bear, E., & Soker, N. 2026, PASP, 138, 034205
Corral-Santana, J. M., Casares, J., Muñoz-Darias, T., et al. 2016, A&A, 587, A61
Dashwood Brown, C., Gandhi, P., & Zhao, Y. 2024, MNRAS, 527, L82
Davis, P. J., Kolb, U., & Knigge, C. 2012, MNRAS, 419, 287
de Kool, M., van den Heuvel, E. P. J., & Pylyser, E. 1987, A&A, 183, 47
De Marco, O., & Izzard, R. G. 2017, PASA, 34, e001
De Marco, O., Passy, J.-C., Moe, M., et al. 2011, MNRAS, 411, 2277
Deng, Z.-L., & Li, X.-D. 2024, ApJ, 971, 54
Deng, Z.-L., Li, X.-D., Shao, Y., & Xu, K. 2024, ApJ, 963, 80
Dewey, R. J., & Cordes, J. M. 1987, ApJ, 321, 780
Di Stefano, R., Kruckow, M. U., Gao, Y., Neunteufel, P. G., & Kobayashi, C. 2023, ApJ, 944, 87
Dominik, M., Belczynski, K., Fryer, C., et al. 2012, ApJ, 759, 52
Dong, Y., García, J. A., Steiner, J. F., & Gou, L. 2020, MNRAS, 493, 4409
Eggleton, P. P. 1983, ApJ, 268, 368
Eggleton, P. P., & Verbunt, F. 1986, MNRAS, 220, 13P
El Mellah, I., Sundqvist, J. O., & Keppens, R. 2019, A&A, 622, L3
Ertl, T., Janka, H. T., Woosley, S. E., Sukhbold, T., & Ugliano, M. 2016, ApJ, 818, 124
Ferguson, J. W., Alexander, D. R., Allard, F., et al. 2005, ApJ, 623, 585
Fortin, F., Kalsi, A., García, F., Simaz-Bunzel, A., & Chaty, S. 2024, A&A, 684, A124
Fragos, T., Andrews, J. J., Ramirez-Ruiz, E., et al. 2019, ApJL, 883, L45
Fragos, T., Willems, B., Kalogera, V., et al. 2009, ApJ, 697, 1057
Gagnier, D., & Pejcha, O. 2025, A&A, 697, A68
Gallegos-Garcia, M., Berry, C. P. L., & Kalogera, V. 2023, ApJ, 955, 133
García-Segura, G., Taam, R. E., & Ricker, P. M. 2020, ApJ, 893, 150
Ge, H., Tout, C. A., Chen, X., et al. 2022, ApJ, 933, 137
Ge, H., Tout, C. A., Chen, X., et al. 2024a, ApJ, 975, 254
Ge, H., Tout, C. A., Webbink, R. F., et al. 2024b, ApJ, 961, 202
Ge, H., Webbink, R. F., Chen, X., & Han, Z. 2020a, ApJ, 899, 132
Ge, H., Webbink, R. F., & Han, Z. 2020b, ApJS, 249, 9
Götberg, Y., Drout, M. R., Ji, A. P., et al. 2023, ApJ, 959, 125
Greene, J., Bailyn, C. D., & Orosz, J. A. 2001, ApJ, 554, 1290
Grichener, A. 2023, MNRAS, 523, 221
Grichener, A., Cohen, C., & Soker, N. 2021, ApJ, 922, 61
Guo, Y., Liu, C., Wang, L., et al. 2022, A&A, 667, A44
Han, Z., Podsiadlowski, P., & Eggleton, P. P. 1994, MNRAS, 270, 121
Han, Z.-W., Ge, H.-W., Chen, X.-F., & Chen, H.-L. 2020, RAA, 20, 161
Hernandez, M. S., Schreiber, M. R., Parsons, S. G., et al. 2022, MNRAS, 512, 1843
Hirai, R., & Mandel, I. 2022, ApJL, 937, L42
Hurley, J. R., Tout, C. A., & Pols, O. R. 2002, MNRAS, 329, 897
Iaconi, R., & De Marco, O. 2019, MNRAS, 490, 2550
Iaconi, R., Reichardt, T., Staff, J., et al. 2017, MNRAS, 464, 4028
Iglesias, C. A., & Rogers, F. J. 1996, ApJ, 464, 943
Ivanova, N. 2002, PhD thesis, University of Oxford
Ivanova, N. 2011, ApJ, 730, 76
Ivanova, N., & Chaichenets, S. 2011, ApJL, 731, L36
Ivanova, N., Justham, S., Chen, X., et al. 2013, A&ARv, 21, 59
Ivanova, N., Justham, S., & Ricker, P. 2020, Common Envelope Evolution (IOP Publishing)
Ivanova, N., & Nandez, J. L. A. 2016, MNRAS, 462, 362
Janka, H.-T. 2012, ARNPS, 62, 407
Janka, H.-T., Melson, T., & Summa, A. 2016, ARNPS, 66, 341
Jermyn, A. S., Bauer, E. B., Schwab, J., et al. 2023, ApJS, 265, 15
Justham, S., Rappaport, S., & Podsiadlowski, P. 2006, MNRAS, 366, 1415
Kiel, P. D., & Hurley, J. R. 2006, MNRAS, 369, 1152
Kippenhahn, R., & Weigert, A. 1990, Stellar Structure and Evolution (Springer)
Klencki, J., Nelemans, G., Istrate, A. G., & Chruslinska, M. 2021, A&A, 645, A54
Klencki, J., Wiktorowicz, G., Gładysz, W., & Belczynski, K. 2017, MNRAS, 469, 3088
Kotko, I., Banerjee, S., & Belczynski, K. 2024, MNRAS, 535, 3577

Kruckow, M. U., Tauris, T. M., Langer, N., Kramer, M., & Izzard, R. G. 2018, MNRAS, 481, 1908
Kruckow, M. U., Tauris, T. M., Langer, N., et al. 2016, A&A, 596, A58
Laplace, E., Justham, S., Renzo, M., et al. 2021, A&A, 656, A58
Laplace, E., Schneider, F. R. N., & Podsiadlowski, P. 2025, A&A, 695, A71
Lau, M. Y. M., Hirai, R., González-Bolívar, M., et al. 2022, MNRAS, 512, 5462
Law-Smith, J. A. P., Everson, R. W., Ramirez-Ruiz, E., et al. 2020, arXiv:2011.06630
Li, X.-D. 2008, MNRAS, 384, L16
Li, X.-D. 2015, NewAR, 64, 1
Li, Z., Jia, S., Wei, D., et al. 2026, ApJL, 996, L42
Liu, Q. Z., van Paradijs, J., & van den Heuvel, E. P. J. 2007, A&A, 469, 807
Liu, Z.-W., Röpke, F. K., & Han, Z. 2023, RAA, 23, 082001
Livio, M., & Soker, N. 1988, ApJ, 329, 764
MacDonald, R. K. D., Bailyn, C. D., Buxton, M., et al. 2014, ApJ, 784, 2
Mapelli, M., Sgalletta, C., Müller-Horn, J., et al. 2026, arXiv:2604.12839
Marchant, P., & Bodensteiner, J. 2024, ARA&A, 62, 21
Marchant, P., Langer, N., Podsiadlowski, P., Tauris, T. M., & Moriya, T. J. 2016, A&A, 588, A50
Marchant, P., Pappas, K. M. W., Gallegos-Garcia, M., et al. 2021, A&A, 650, A107
Meibom, S., & Mathieu, R. D. 2005, ApJ, 620, 970
Mirabel, F. 2017, NewAR, 78, 1
Moe, M., & Di Stefano, R. 2017, ApJS, 230, 15
Moreno, M. M., Schneider, F. R. N., Röpke, F. K., et al. 2022, A&A, 667, A72
Motta, S. E., Belloni, T. M., Stella, L., Muñoz-Darias, T., & Fender, R. 2014, MNRAS, 437, 2554
Müller, B., Viallet, M., Heger, A., & Janka, H.-T. 2016, ApJ, 833, 124
Nagarajan, P., & El-Badry, K. 2025, PASP, 137, 034203
Naoz, S., Fragos, T., Geller, A., Stephan, A. P., & Rasio, F. A. 2016, ApJL, 822, L24
Nathaniel, K., Langer, N., Simón-Díaz, S., et al. 2025, A&A, 702, A197
Nelemans, G., Preece, H., Temmink, K., Munday, J., & Pols, O. 2025, A&A, 700, A219
Nelemans, G., & Tout, C. A. 2005, MNRAS, 356, 753
Nelemans, G., Verbunt, F., Yungelson, L. R., & Portegies Zwart, S. F. 2000, A&A, 360, 1011
Nie, J. D., Wood, P. R., & Nicholls, C. P. 2017, ApJ, 835, 209
Nie, Y.-D., Shao, Y., He, J.-G., et al. 2025, ApJ, 979, 112
Ogilvie, G. I. 2014, ARA&A, 52, 171
Ohlmann, S. T., Röpke, F. K., Pakmor, R., & Springel, V. 2016, ApJL, 816, L9
Orosz, J. A. 2003, IAUS, 212, 365
Orosz, J. A., & Bailyn, C. D. 1997, ApJ, 477, 876
Orosz, J. A., Jain, R. K., Bailyn, C. D., McClintock, J. E., & Remillard, R. A. 1998, ApJ, 499, 375
Orosz, J. A., Kuulkers, E., van der Klis, M., et al. 2001, ApJ, 555, 489
Paczynski, B. 1976, IAUS, 73, 75
Paxton, B., Bildsten, L., Dotter, A., et al. 2011, ApJS, 192, 3
Paxton, B., Cantiello, M., Arras, P., et al. 2013, ApJS, 208, 4
Paxton, B., Marchant, P., Schwab, J., et al. 2015, ApJS, 220, 15
Paxton, B., Schwab, J., Bauer, E. B., et al. 2018, ApJS, 234, 34
Paxton, B., Smolec, R., Schwab, J., et al. 2019, ApJS, 243, 10
Pfahl, E., Rappaport, S., & Podsiadlowski, P. 2003, ApJ, 597, 1036
Picker, L., Hirai, R., & Mandel, I. 2024, ApJ, 969, 1
Podsiadlowski, P., Ivanova, N., Justham, S., & Rappaport, S. 2010, MNRAS, 406, 840
Podsiadlowski, P., Rappaport, S., & Han, Z. 2003, MNRAS, 341, 385
Postnov, K. A., & Yungelson, L. R. 2014, LRR, 17, 3
Rebassa-Mansergas, A., Zorotovic, M., Schreiber, M. R., et al. 2012, MNRAS, 423, 320
Repetto, S., & Nelemans, G. 2015, MNRAS, 453, 3341
Röpke, F. K., & De Marco, O. 2023, LRCA, 9, 2
Sana, H., de Mink, S. E., de Koter, A., et al. 2012, Sci, 337, 444
Scherbak, P., & Fuller, J. 2023, MNRAS, 518, 3966
Schneider, F. R. N., Laplace, E., & Podsiadlowski, P. 2025, A&A, 700, A253
Schneider, F. R. N., Podsiadlowski, P., & Laplace, E. 2023, ApJL, 950, L9
Schneider, F. R. N., Podsiadlowski, P., & Laplace, E. 2024, A&A, 686, A45
Schneider, F. R. N., Podsiadlowski, P., & Müller, B. 2021, A&A, 645, A5
Scolnic, A., Bear, E., & Soker, N. 2025, PASP, 137, 034201
Shafee, R., McClintock, J. E., Narayan, R., et al. 2006, ApJL, 636, L113
Shahbaz, T. 2003, MNRAS, 339, 1031
Shao, Y. 2022, RAA, 22, 122002
Shao, Y., & Li, X.-D. 2015, ApJ, 809, 99
Shariat, C., Naoz, S., El-Badry, K., et al. 2025, ApJ, 983, 115
Shiber, S., & Iaconi, R. 2024, MNRAS, 532, 692
Shiber, S., Iaconi, R., De Marco, O., & Soker, N. 2019, MNRAS, 488, 5615
Shiber, S., & Soker, N. 2018, MNRAS, 477, 2584
Soker, N. 2004, NewA, 9, 399
Soker, N. 2015, ApJ, 800, 114
Soker, N. 2016, NewAR, 75, 1
Soker, N. 2025, RAA, 25, 025023
Sørensen, M., Fragos, T., Steiner, J. F., et al. 2017, A&A, 597, A12
Stancliffe, R. J., Fossati, L., Passy, J. C., & Schneider, F. R. N. 2015, A&A, 575, A117
Sukhbold, T., Ertl, T., Woosley, S. E., Brown, J. M., & Janka, H. T. 2016, ApJ, 821, 38
Tanaka, A. M., Gilkis, A., Izzard, R. G., & Tout, C. A. 2023, MNRAS, 522, 1140
Tauris, T. M., Fender, R. P., van den Heuvel, E. P. J., Johnston, H. M., & Wu, K. 1999, MNRAS, 310, 1165
Tauris, T. M., & van den Heuvel, E. P. J. 2006, in Compact Stellar X-Ray Sources, ed. W. Lewin & M. van der Klis (Cambridge Univ. Press)
Tauris, T. M., & van den Heuvel, E. P. J. 2023, Physics of Binary Star Evolution: From Stars to X-ray Binaries and Gravitational Wave Sources (Princeton Univ. Press)
Tetarenko, B. E., Sivakoff, G. R., Heinke, C. O., & Gladstone, J. C. 2016, ApJS, 222, 15
Torres, S., Gili, M., Rebassa-Mansergas, A., et al. 2025, A&A, 698, A173
Ugliano, M., Janka, H.-T., Marek, A., & Arcones, A. 2012, ApJ, 757, 69
Vartanyan, D., Laplace, E., Renzo, M., et al. 2021, ApJL, 916, L5
Verbunt, F., Wijers, R. A. M. J., & Burm, H. M. G. 1990, A&A, 234, 195
Vetter, M., Röpke, F. K., Schneider, F. R. N., et al. 2025, A&A, 698, A133
Vigna-Gómez, A., Wassink, M., Klencki, J., et al. 2022, MNRAS, 511, 2326
Vink, J. 2012, A&ARv, 20, 49
Vink, J. S. 2022, ARA&A, 60, 203
Wang, C., Jia, K., & Li, X.-D. 2016a, RAA, 16, 126
Wang, C., Jia, K., & Li, X.-D. 2016b, MNRAS, 457, 1015
Wang, S., Zhao, X., Feng, F., et al. 2024, NatAs, 8, 1583
Webbink, R. F. 1984, ApJ, 277, 355
Wei, D., Schneider, F. R. N., Podsiadlowski, P., et al. 2024, A&A, 688, A87
Weiner, Y., & Soker, N. 2025, RAA, 25, 115014
Wiktorowicz, G., Belczynski, K., & Maccarone, T. 2014, in Binary Systems, their Evolution and Environments, 37
Willems, B., Henninger, M., Levin, T., et al. 2005, ApJ, 625, 324
Wilson, E. C., & Nordhaus, J. 2022, MNRAS, 516, 2189
Wong, T.-W., Valsecchi, F., Ansari, A., et al. 2014, ApJ, 790, 119
Wong, T.-W., Valsecchi, F., Fragos, T., & Kalogera, V. 2012, ApJ, 747, 111
Woosley, S. E. 2019, ApJ, 878, 49
Xu, X.-J., & Li, X.-D. 2010, ApJ, 716, 114
Yamaguchi, N., El-Badry, K., Rees, N. R., et al. 2024, PASP, 136, 084202
Yang, Z. L., Han, J. L., Zhou, D. J., et al. 2025, Sci, 388, 859
Yungelson, L. R., Lasota, J. P., Nelemans, G., et al. 2006, A&A, 454, 559
Zhang, Y., Li, Z., Chen, X., & Han, Z. 2024, ApJ, 977, 24
Zhao, Y., Gandhi, P., Dashwood Brown, C., et al. 2023, MNRAS, 525, 1498
Zorotovic, M., & Schreiber, M. 2022, MNRAS, 513, 3587
Zorotovic, M., Schreiber, M. R., Gänsicke, B. T., & Nebot Gómez-Morán, A. 2010, A&A, 520, A86
Zou, Y., Chamandy, L., Carroll-Nellenback, J., Blackman, E. G., & Frank, A. 2022, MNRAS, 514, 3041
Zuo, Z.-Y., & Li, X.-D. 2014, ApJ, 797, 45